A flexible two-photon fiberscope for fast activity imaging and precise optogenetic photostimulation of neurons in freely moving mice

Nicolò Accanto, François G.C. Blot, Antonio Lorca-Cámara, Valeria Zampini, Florence Bui, Christophe Tourain, Noam Badt, Ori Katz, Valentina Emiliani

A flexible two-photon fiberscope for fast activity imaging and precise optogenetic photostimulation of neurons in freely moving mice

Nicolò Accanto[1*], François G. C. Blot[1*], Antonio Lorca-Cámara[1*], Valeria Zampini[1], Florence Bui[1], Christophe Tourain[1], Noam Badt[2], Ori Katz[2], and Valentina Emiliani[1,3]

[1] Sorbonne Université, INSERM, CNRS, Institut de la Vision, F-75012 Paris, France

[2] Department of Applied Physics, Hebrew University of Jerusalem, Jerusalem 9190401, Israel.

[3]Lead Author

* These authors contributed equally

Contact: nicolo.accanto@inserm.fr, valentina.emiliani@inserm.fr

Abstract

We developed a flexible two-photon microendoscope (2P-FENDO) capable of all-optical brain interrogation at near cellular resolution in freely moving mice. The system performs fast two-photon (2P) functional imaging and 2P holographic photostimulation of single and multiple cells using axially confined extended spots. Proof-of-principle experiments were performed in freely moving mice co-expressing jGcaMP7s and the opsin ChRmine in the visual or barrel cortex. On a field of view of 250 μm in diameter, we demonstrated functional imaging at a frame rate of up to 50 Hz and precise photostimulation of selected groups of cells. With the capability to simultaneously image and control defined neuronal networks in freely moving animals, 2P-FENDO will enable to precisely define the functions of neurons in the brain and their interactions during naturalistic behaviours.

Introduction

A key question in neuroscience is to understand the links between neuronal activity and behavior. This complicated task demands powerful tools to map activity patterns and precisely manipulate selected neurons in the brain circuits of living and freely behaving animals[1]. Combined advances in multiphoton-microscopy and optogenetic sensors and actuators, have provided the technology for *in vivo*, single cell precise, all-optical imaging and optogenetic manipulation of neuronal circuits in head-restrained animals [2–10]. The next essential step is to extend such technologies to the study of brain circuits in animals that can freely perform behavioral tasks engaging the circuits of interest. If several systems were previously reported for imaging neuronal activity in freely moving rodents[11–19], a precise optogenetic photo-stimulation approach allowing to manipulate neuronal activity at the single cell level during natural behavior is still missing.

Current systems capable of imaging in freely moving rodents can be grouped into three main categories: one-photon (1P) head-mounted wide-field microscopes; two- or three-photon (2P, 3P) systems coupled to a single optical fiber with a portable scanning unit attached to the animal head; 1P or 2P systems based on a bundle of optical fibers in which the scanning and beam manipulation unit is placed before the bundle.

1P head-mounted miniaturized microscopes (or miniscopes) come with a simple optical set up and, due to their wide field illumination, can perform functional imaging of large fields of view (FOV) (up to ~1mm^2) at high acquisition frame rates (20-100 Hz) [11,20]. However, their lack of optical sectioning produces relatively high background fluorescence, and 1P excitation limits the imaging depth to few tens of μm below the miniscope objective lens.

2P or even 3P miniaturized-microscopes[14,15,19,21–27] generally use a single optical fiber as a point source and a miniaturized scanning unit, attached to the animal skull, to scan the excitation light across the focal plane. These systems outperform 1P miniscopes in optical resolution and penetration depth, enabling high quality recordings[27] up to 40 Hz on FOVs of 400x400 μm^2.

Optogenetic manipulation in freely moving animals using the previous approaches remains challenging. Different 1P miniscope versions were combined with wide-field photostimulation of the same[28] or different[13] brain areas with respect to the imaging FOV, but lacked cellular resolution. Recently, a newer system[29] incorporated a digital micromirror device (DMD) for 1P patterned photostimulation, but only achieved a penetration depth of ~ 30 μm and an axial resolution of 30 μm. On the other hand, multi-photon miniaturized-microscopes, where light is delivered on the sample through a single optical fiber are not compatible with the simultaneous generation of patterned light for multi-target optogenetic photo-stimulation.

Alternatively, patterned illumination can be reached by using a fiber bundle microscope[16–18,30], in which a bundle of optical fibers relays a regular-sized microscope to the animal head. Such an approach broadens the capabilities of the system and makes it compatible with advanced optical techniques, such as computer-generated holography. A first fiber bundle microscope combined with 1P-structured illumination and 1P-holographic light patterning could indeed perform optogenetic photo-stimulation with near cellular resolution, in freely moving mice. However, the use of 1P excitation with short penetration depth, the large size and the short working distance of the micro-objective limited this approach to the shallow depth of 60 μm[16]. Larger penetration depths and better axial sectioning in fiber bundle microscopes could be reached by replacing 1P with 2P excitation[18,31]. However, in this case, the difficulty in propagating high energy laser pulses through fiber bundles, limited the imaging speed[18] to 2.5 Hz on a FOV of ~200 x 200 μm^2. Most importantly, 2P optogenetic photostimulation through a fiber bundle-based microscope has not yet been demonstrated.

In this work we overcome these limitations by developing a flexible two-photon endoscope (2P-FENDO) based on a fiber bundle and a gradient index (GRIN) lens for fast 2P functional imaging and 2P holographic photostimulation of single and multiple cells in freely moving animals. To achieve this, we make use of extended and more efficient 2P excitation spots for both imaging and photostimulation and demonstrate that, by exploiting the intrinsic inter-core delay dispersion of the fiber bundle, 2P-FENDO keeps single cell axial resolution independently of the

size of the excitation spots. Using mice injected with ChRmine and jGCaMP7s in the visual and barrel cortex, we demonstrated functional imaging at up to 50 Hz on a FOV of 250 µm in diameter, at a depth of up to 150 µm and, for the first time, 2P multi-target photostimulation in freely moving animals.

Results

Inter core delay dispersion and optical axial resolution characterization

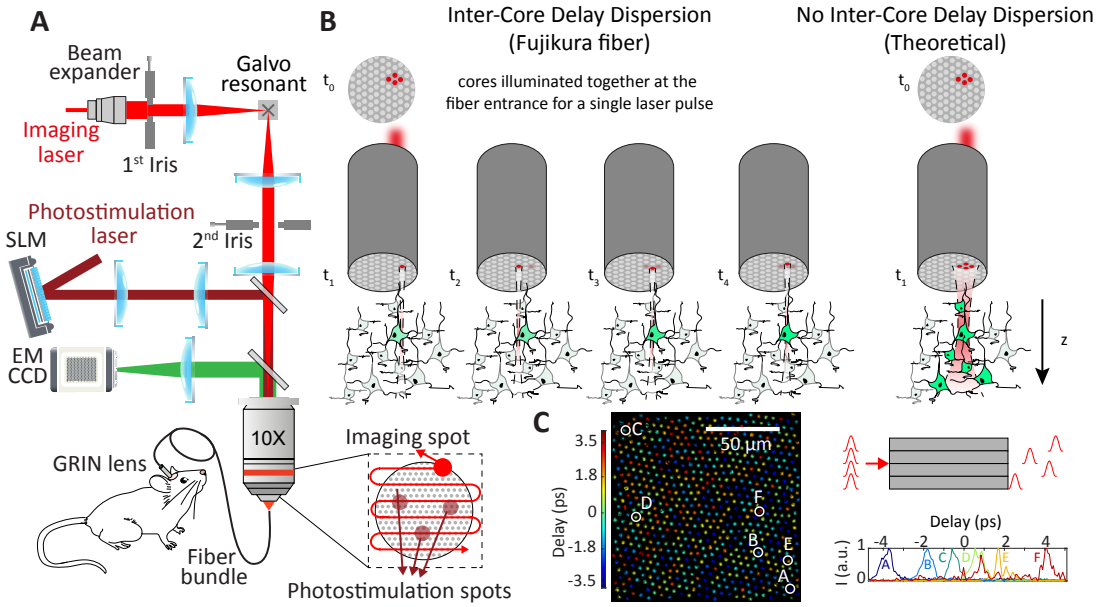

Figure 1. Optical set-up of the flexible two-photon endoscope (2P-FENDO). *A) Schematics of the optical setup.* ***B)*** *Representation of the effect of the inter-core delay dispersion on the axial sectioning capabilities for an extended excitation spot. Left: through the Fujikura fiber bundle the incoming laser pulse simultaneously illuminates different cores at t_0, but is outcoupled from each core at slightly different times (t_1 to t_4). As the pulses from each core do not interact with each other at the sample, the axial resolution corresponds to the single core axial resolution, which ensures imaging and photostimulation with single cell axial confinement. Right: through a theoretical fiber bundle with no inter-core delay dispersion, the laser pulses from each core are outcoupled simultaneously and interact at the sample, resulting a much worse axial confinement.* ***C)*** *Measurement and scheme of the delays experienced by a laser pulse when propagating through multiple cores of a 60 cm Fujikura fiber bundle (see* ***Supplementary Figure 1****).*

The optical setup (**Fig. 1A** and **Methods** for details) consists of two different optical paths for imaging and photo-stimulation. The imaging laser is an ultrafast fiber laser (Alcor, Spark Lasers) that is scanned by a galvo-resonant scanner at the entrance of the fiber bundle. The photostimulation laser is a low repetition rate fiber laser (Goji, Amplitude) that is spatially shaped by a SLM (Hamamatsu) using computer-generated holography (CGH) to generate single or multiple excitation spots at the imaging plane. The imaging and photo-stimulation lasers are focused by a 0.3 NA objective at the entrance of the endoscope. The micro-endoscope is composed of a 2-m long fiber bundle (Fujikura, diameter of 550 μm, 15000 fiber cores) and a commercial, chromatic and field corrected GRIN lens (Grintech, diameter of 1.3 mm) placed above the cranial window. In practice, the GRIN lens behaves like a doublet, re-imaging the output facet of the fiber bundle at the sample plane (see **Supplementary Fig.1**) with a certain magnification factor (see **Table 1**).

High-speed 2P imaging is achieved by scanning with a galvo-resonant scanner an excitation spot of variable size, at the entrance of the fiber bundle. A motorized iris on the path to the fiber bundle is used to change the imaging spot size and thus the total amount of power at the focal plane so to keep the power/core < 10 mW, which corresponds to the threshold for nonlinear effects, such as self-phase modulation (SPM) to occur [31–35]. SPM has the detrimental effect of decreasing the wavelength bandwidth transmitted by the fiber, thus increasing the pulse length and decreasing the 2P excitation efficiency, and cannot be easily compensated for. The emitted fluorescence is collected through the same GRIN objective + fiber bundle system, separated from the laser light using a dichroic mirror, and detected by a high yield EM-CCD camera (Andor IXon Ultra 888).

Single or multi target photo-stimulation is achieved by projecting at the entrance of the fiber bundle a two-dimensional distribution of holographic spots generated by a SLM placed at the Fourier plane of the microscope objective pupil.

To increase imaging speed and photostimulation efficiency, 2P-FENDO uses excitation spots of 10-20 μm in diameter for imaging, and 10 μm in diameter for photo-stimulation (matching the size of a neuron). In a classical optical setup, this would result in a drastic loss in axial resolution, which could undermine the

advantages of using 2P excitation. As illustrated in **Fig. 1B-C**, 2P-FENDO circumvents this problem by taking advantage of the pulse propagation properties inside the fiber bundle.

	Input NA	Output NA	M	Input Work. Dist. (µm)	Output Work. Dist. (µm)	GRIN diameter (mm)	FOV diameter (µm)	Lateral res. (µm)
GRIN 1 GT-MO-070-016-ACR-VISNIR-30-20	0.16	0.7	4.5	200	300, not corrected for cover glass	1.3	122, limited by bundle diameter	~ 1, limited by inter-core distance
GRIN 2 GT-MO-080-032-ACR-VISNIR-08CG-20	0.32	0.7	2.2	200	80, below 170 µm cover glass	1.3	250, limited by bundle diameter	~ 2, limited by inter-core distance

Table 1. Parameters of the two GRIN lenses. *Input/output NA refer to the numerical aperture of the GRIN lenses on the fiber and sample side respectively. M is the magnification of the GRIN lens. Input and output working distances refer to the nominal working distance of the GRIN lenses on the fiber and sample side respectively. Input (output) working distances are specified for air (water) immersion respectively. Both GRIN lenses are suitable for imaging through a cover glass on the sample side, even if GRIN 1 is not specifically designed for that. The field of view and lateral resolution depend on the physical size of the fiber bundle (550 µm in diameter, 15000 total cores), its core-to-core distance (~ 4.5 µm), and on the magnification of the GRIN lens, in the way described in* ***STAR Methods****.*

Fujikura fiber bundles[36], as well as bundles of different types[37], generally present a certain degree of core-to-core variation in size and shape. This results in an inter-core delay dispersion (ICDD), meaning that pulses coupled at the same time through different cores arrive at the sample plane at slightly different times, thus decreasing the out of focus 2P interaction with one another (**Fig. 1B**). We quantified this effect by interferometric measurements (**Fig. 1C** and **Supplementary Fig. 1A)** in which an ultrafast pulse from a Ti:sapph laser was

split into two arms. One arm was sent through the fiber bundle, and the reference arm was delayed using an adjustable delay line. Using off-axis optical coherent tomography[38] and demodulation, we extracted the time cross-correlation of the reference arm and the fiber bundle arm. Since we imaged the fiber onto a camera, we effectively measured the electric field on each core separately. This technique allowed us to differentiate between different modes in each core by using a spatial filter applied to each core in post-processing, and therefore to selectively measure the arrival time of the pulse in the first mode.

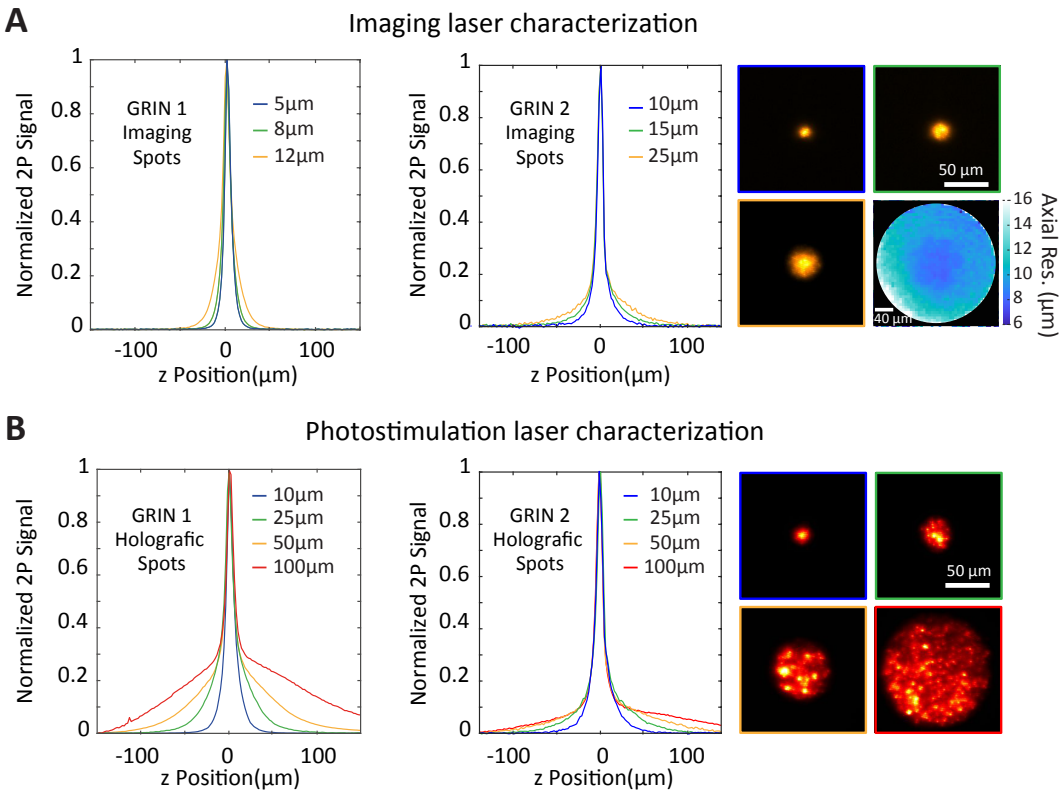

Figure 2. Axial resolutions characterization. *Axial resolution measurements for extended spots of different sizes for the imaging (**A**) and photostimulation (**B**) lasers respectively and for the two different GRIN lenses (left: GRIN 1, right: GRIN2). In the case of the imaging laser, the different spot sizes were obtained with different apertures of the motorized iris, for the photostimulation laser, they correspond to different sizes of the holographic spots produced by the SLM. The axial resolutions were measured by moving the distal end of the fiber plus the GRIN lens together in z using a vertical step motor while recording the emitted 2P fluorescence from a thin (~ 1 µm) rhodamine layer with the camera detector. The space between the GRIN lens and the rhodamine layer was filled with water, i.e. the GRIN lens was used in water immersion conditions. The axial full width at half maximum of the central Lorentzian peaks is as narrow as 7 µm for the imaging laser*

*and 9 µm for the photostimulation one. The two-dimensional images on the excitation spots on the right were acquired with GRIN2 (see Table 1). In **A**) the bottom right image represents the position-dependent axial resolution, calculated as the full width at half maximum of the Lorentzian peak, for a 15 µm imaging spot that was raster scanned across the whole fiber bundle. The axial resolution is ~7 µm at the center and increases to ~ 13 µm at the edges of the FOV. The indicated spot sizes refer to the spot at the sample plane. For subsequent experiments the imaging spot size was maintained below 20 µm which does not affect the resolution (see **Supplementary Figure 2**).*

We found that the measured average ICDD for different types of Fujikura fibers is in the range of 1 to 2 ps/m. With our imaging and photostimulation lasers both producing pulses of ~150 fs, we experimentally confirmed that after propagation through 2 m of fiber, such ICDD values are sufficient to decouple in time the different cores, thus maintaining good axial resolution even for large 2P excitation spots (**Fig. 2**). We measured the axial profile for two different GRIN lenses with high numerical aperture (NA) on the sample side and with chromatic and field corrections. The parameters of the two GRIN lenses are listed in **Table 1**. The axial profiles are dominated by a narrow central Lorentzian peak of full width at half maximum (FWHM) of 7-9 µm. As the 2P spots are made larger, (> 50 µm; **Fig. 1d**) a broader pedestal starts to appear, which might result in out of focus excitation. To understand the physical origin of the pedestal, one can think that, as the excitation spot becomes larger, more fiber cores are simultaneously illuminated, which increases the probability that pulses from different cores will experience similar temporal delays, thus contributing to out of focus excitation. To avoid the consequent loss of axial sectioning, we always kept the imaging and photostimulation spots at a diameter < 20 µm, which for both GRIN lenses was unaffected by the pedestal component (see **Supplementary Fig. 2**).

In vivo and in vitro depth resolved imaging with different GRIN lenses We first assessed the capability of 2P-FENDO, with the two different GRIN lenses, to image fixed non-scattering samples (pollen grains, **Fig. 3A**), scattering samples (fixed brain slices, **Fig. 3B**, first and third row), and *in vivo* TdTomato and jGCaMP7s expressing neurons in head-fixed and anesthetized mice (**Fig. 3B**, second and forth row) with axial sectioning. For that, we acquired *z* stacks of the

selected samples by moving together the fiber bundle and the GRIN lens, with a *z* step motor, relative to the brain surface (**Fig. 3B**).

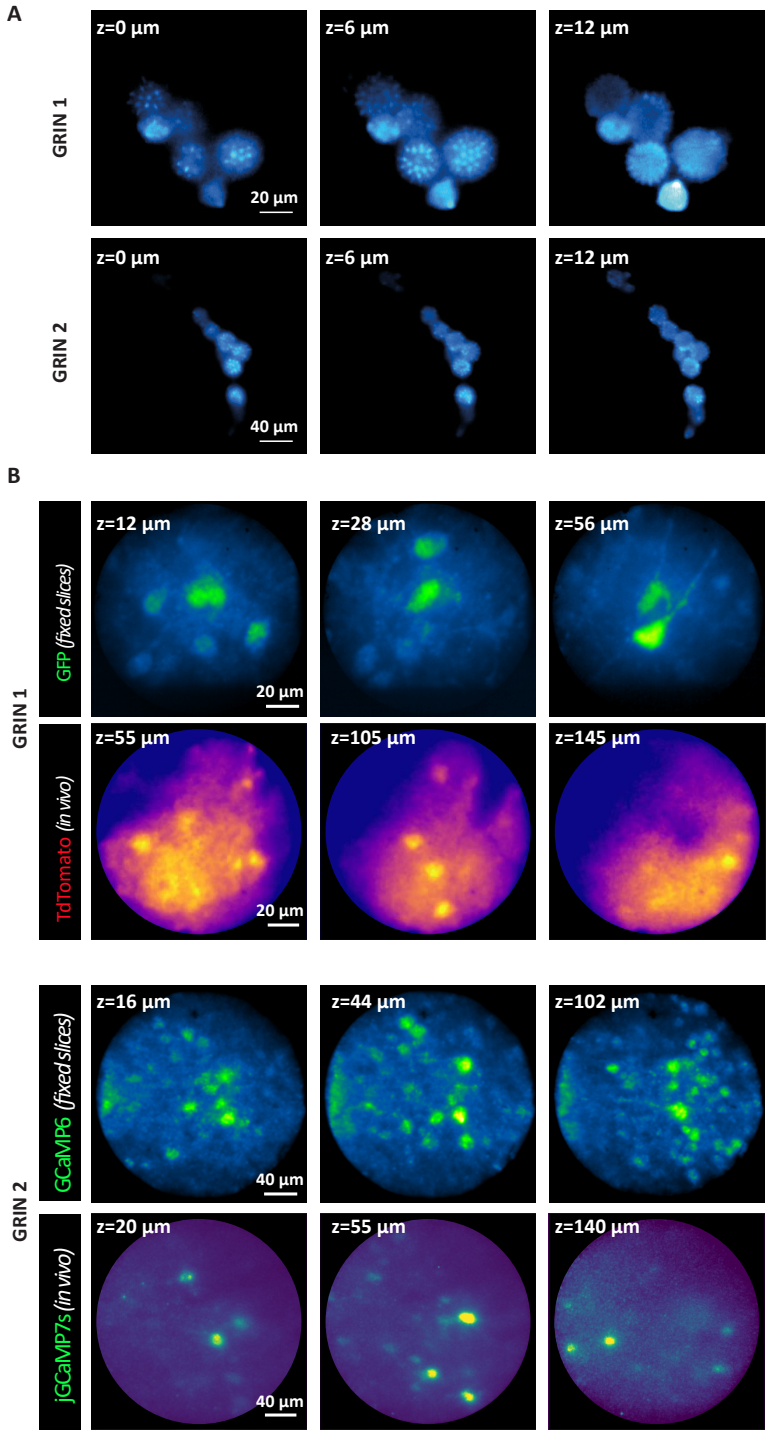

Figure 3. Imaging capabilities of 2P-FENDO. *A) 2P z-stacks of pollen grains with two different GRIN lenses. B). Upper panel: 2P z-stacks with GRIN1 of GFP labelled hippocampal brain slices (upper row) and in vivo TdTomato labelled cortical neurons in injected mouse*

(lower row). Lower panel: 2P z-stacks with GRIN2 of GCaMP6 labelled cortical brain slices (upper row) and in vivo jGCaMP7s labelled cortical neurons in injected mouse (lower row). GFP and jGCaMP7s labelled neurons were imaged with 920 nm laser and TdTomato with 1040 nm laser. Because of the higher magnification of GRIN1, the sharp edges of pollen grains as well as neuronal processes are clearly visible, whereas with GRIN2 we have access to a twice bigger FOV. For example z-stacks see ***Suppl. Video 1.***

The main difference between the two GRIN lenses is the magnification (M in **Table 1**) and thus the size of the FOV (122 μm and 250 μm respectively) and the lateral resolution (~1 μm and ~2 μm respectively). GRIN 1 has higher lateral resolution, it is thus more adapted to see small features at the sample, with a FOV limited to a diameter of 125 μm (**Fig. 3A-B upper panels**). GRIN 2 offers larger FOVs (250 μm in diameter) with lower resolution that still allows to discriminate individual cells (**Fig. 3A-B lower panels**, see **STAR Methods** for a detailed explanation). As better explained in **STAR Methods** and illustrated in **Supplementary Fig. 3**, to extend the working distance of the GRIN lenses below the cranial window for experiments *in vivo*, we always placed the GRIN lens in contact with the fiber bundle (i.e., at a smaller distance with respect to the input working distance, see **Table 1**) and used protected cover glasses on top of the brain surface of a thickness of ~100 μm, which is ~70 μm smaller than the cover glasses the GRIN lenses are designed for. This resulted in sufficient working distance to image at depths of 150-200 μm through the cover glass with minor added aberrations.

We also demonstrated morphological imaging of TdTomato expressing neurons through 2P-FENDO by using a 1040 nm fiber laser (**Fig. 3B**). This opens the possibility for functional imaging of red shifted calcium indicators[39], which would not be efficiently excited by a 920 nm laser.As **Fig. 3** demonstrates, in all cases, the good axial confinement produced by the ICDD of the Fujikura fiber enabled achieving a good optical sectioning (for the complete stack data, see **Supplementary videos 1**), even in fixed highly scattering samples (brain slices) and most importantly for *in vivo* imaging.

In vivo functional calcium imaging in freely moving animals

We assessed the capability of 2P-FENDO to perform functional calcium imaging at the highest achievable speed and optogenetic photostimulation *in vivo* in freely

moving mice, with small movement artifacts, excellent long term stability and without obstructing animals' free motions (**Fig. 4-6**). For the following experiments we always used GRIN 2, which gives access to a larger FOV. We co-injected an AAV9 viral vector for jGCaMP7s [40] expression together with an AAV1 vector for expression of the opsin ChRmine (AAV1.hSyn.ChRmine.mScarlet.Kv2.1.WPRE, see Ref. [3]), both under h-synapsin promoter, delivered by stereotaxic injections in primary visual cortex (V1) or primary somatosensory barrel cortex (wS1). Four to eight weeks post injection, the cranial window surgery was performed under ketamine/xylazine anesthesia and the animals were given at least 3 days of recovering before the first day of imaging. For experiments in freely moving animals, we used a custom made, lightweight (Impl.1/2/3 + joint=0.7g, **Fig. 4E**) holder for the fiber and the GRIN lens that could be attached to the mouse head. The implant was positioned over the cranial window of the head fixed animal maintained under isoflurane anesthesia, on the first day of the imaging sessions. Once a region of interest was identified, the implant was cemented over the window and experiments were performed in the hours following the surgery (see **Methods** for details on preparations). The fiber bundle was then removed at the end of each session and inserted back in the following days to repeat experiments on the same FOV. For all the freely moving experiments, the space between the GRIN lens tip and the cranial window was filled with index matching oil for microscope objectives, to prevent easy evaporation that would happen in case of water immersion. As shown in **Supplementary Fig. 3**, and discussed in **STAR Methods**, this had the result of moving the actual focal plane of few μm towards the brain surface, with neglectable other effects on the optical properties.

In successive experimental days, the animal was maintained 20-30 min under isoflurane anesthesia to position the fiber in the implant. Each experiment was spaced of at least 3 days to allow for the recovery of the animal.

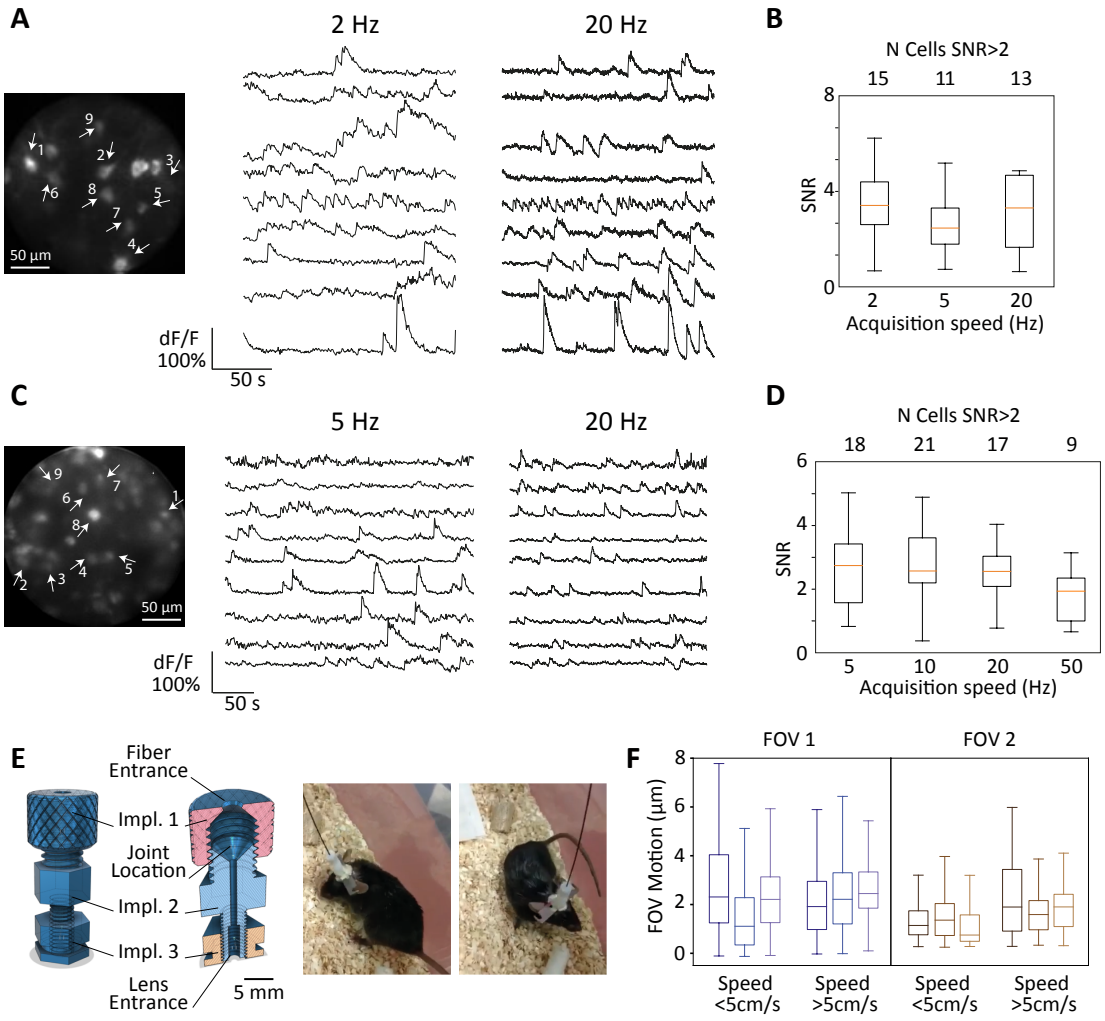

Figure 4. Imaging of spontaneous calcium activity in freely moving mice. ***A*** *&* ***C****. Two representative FOVs in two different mice with corresponding calcium transients (dF/F) for 9 selected cells for each FOV imaged at low (2 or 5 Hz) and high (20 Hz) acquisition speeds. Imaging power and spot size were 135 mW and 16 µm at all the imaging rates.* ***B*** *&* ***D****. SNR quantification and number of cells with SNR higher than 2 for the two FOVs as a function of the acquisition speed.* ***E****. Image of the implant, a lightweight, simple to produce and cost-effective holder for the fiber and the GRIN lens. This implant is composed of three elements carved from a nylon screw (RS Pro, nylon, douille hexagonale mâle/femelle, 30 mm, M4 x M, RS code: 325-801), assembled with a joint (****HLC-11*** *orange cone washer). The fiber (0.65 mm outer diameter) passes in the first element of the implant (Impl.1), through an opening of 0.7mm, then through the joint (1.1 mm inner diameter), and halfway through the second element (Impl.2). Once the Impl.1 and 2 are screwed together the joint compresses to clench the fiber within the implant. The GRIN lens (1.3 mm outer diameter) is introduced in the Impl.2 from the other end, to come directly in contact with the fiber. The openings of Impl.2 are centered for the optimal alignment of the fiber and the lens. A third element (Impl.3)*

screws onto Impl.2 to act as a chuck, clenching the lens in position. The fully assembled implant was positioned over the cranial window of the anesthetized/head fixed animal, performed as previously described. Once a region of interest is identified, the implant is cemented over the window. Impl.3 is the sole element to be permanently fixed onto the animal's head, thus allowing to make the system fully detachable by unscrewing Impl.2 from Impl.3. The relative position of Impl.2 in Impl.3 also changes the distance between the lens and the sample, allowing to manually change the focal plan of imaging. The total weight of the implant (Impl.1/2/3 + joint) is 0.7g. Scale bar = 5mm. Representation images of a mouse in its cage with the implant and the fiber bundle fixed on the head. ***F****. Quantification of the lateral non-rigid motion of the FOV for three different acquisitions (different color hues) of total duration of 300 s in 2 representative FOVs of animals #1/2, see* ***Supplementary Table1****, for low (< 5cm/s) and high (> 5cm/s) movement speed of the mouse in the cage. Acquisition examples are presented in* ***Suppl. Video 2****.*

We first characterized the imaging properties of 2P-FENDO by measuring the spontaneous activity of jGCaMP7s expressing neurons in freely moving mice (**Fig. 4 and Supp. Video 2**). The recordings were performed in cortical superficial layers (between 70 µm and 150 µm from the brain surface) at different imaging frame rates (from 2Hz to 50 Hz), with powers ranging from 85 to 155 mW (see **Supplementary Table1**).

We used a semi-automatized analysis (see **Methods**) based on CaImAn[41], a software for calcium imaging data analysis, to correct for motion artefacts, select regions of interest (ROIs), extract the calcium traces (corrected for neuropil activity and with baseline subtraction, DF/F signal), and quantify the signal to noise ratio (SNR). As shown in the exemplary graphs of **Fig. 4A-D** (5 different measurement days on 3 different mice), we were consistently able to detect calcium transients in multiple neurons with reliable SNR at acquisition frame rates as high as 20 Hz. A significant drop in the SNR occurred when trying to image at the frame rate of 50 Hz (**Fig. 4 D**) with consequent losses of detectable cells, indicating that more laser power, or different imaging strategies (see **Discussion**) should be used to achieve higher frame rates.

Video recordings of the mouse in the cage were simultaneously acquired during the calcium imaging acquisitions, which allowed us to correlate the motion artefacts of the FOV with the movements of the animal and the relative speed,

obtained by analyzing the videos of the mice with DeepLabCut[42]. For each frame in the acquisition (total duration of 300s per acquisition), we estimated the average motion of the FOV by using the resulting values of the planar non-rigid motion correction algorithm of CaImAn[41] (see **Methods**). In **Fig. 4F** we report the average motion artefacts over the acquisition periods in which the animal was moving in the cage at lower (< 5 cm/s) or higher (> 5 cm/s) speeds. Motion artefacts were on average around 2 µm, with peaks that could reach 8 µm for a short time, and a slight tendency on some cases (such as in **Fig. 4F**, FOV2) to increase when the mouse was moving at higher speeds.

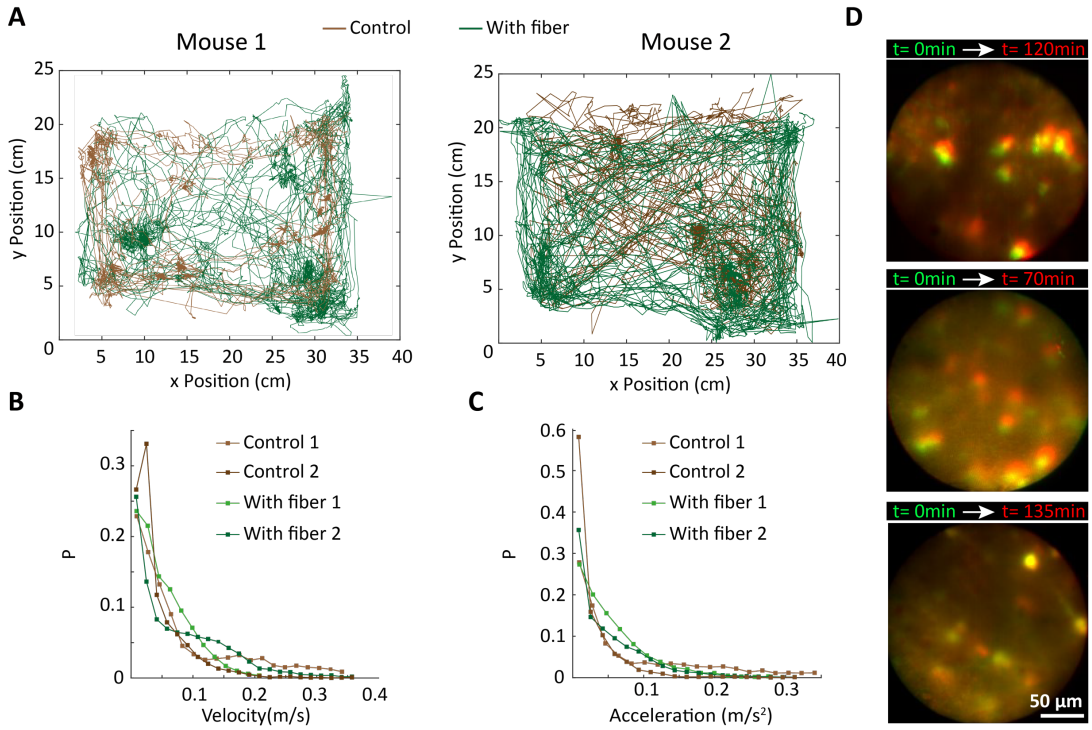

Figure 5. Mice movement with or without fiber, and long-term stability of the implant. A*. Position tracking of two different mice for a time of 10-20 minutes, when the fiber bundle was in the implant and, on a different day, without the fiber bundle (only with headplate and implant, called control in figure). In all cases animals were anesthetised for 20 minutes with isoflurane to have the same starting conditions.* ***B-C****. Probability distribution of the mouse velocity and acceleration showing no significant difference between the control (with no fiber) and with fiber condition.* ***D****. Examples FOVs of long time (> 1h) in 3 different mice in freely moving conditions to illustrate stability of the FOV. Each image is the superposition of two images, one acquired at the beginning (in green) and one at the end (in red) of the experimental session. The total displacement over the entire session is < 20 µm.*

A critical property that a head mounted system should demonstrate is its capability to allow recordings in moving animals without restricting their locomotion. To confirm that the fiber bundle did not hamper free movements or alter normal behavior we recorded trajectories, speeds and accelerations for different animals with and without the attached fiber. The results are shown in **Fig. 5A-C**, from which one can clearly deduce a similar level of locomotion for the control and implanted animals. Finally, as Fig. 5D demonstrates, with the described implant, we could reliably perform optical experiments for hours with a relatively stable FOV.

In vivo holographic photostimulation in freely moving animals

We next demonstrated the capability of 2P-FENDO to perform, for the first time, high resolution 2P photostimulation of a single or multiple targets in freely moving mice. After acquiring a reference image of the FOV, we selected the single or multiple neurons to target and generated with the SLM the corresponding holograms which also contained the corrections to achieve uniform light distribution across the FOV (**Supplementary Fig. 4A-B**). Precisely, the SLM diffraction efficiency, but most importantly the residual aberration of the GRIN lens [43–45], caused a marked decrease of the two-photon fluorescence (2PF) on the edges of the FOV. To compensate for this, we generated corrected holograms to send more laser power to off-centered holographic spots (~ 2 times more than in the center), which resulted in uniform 2PF emitted from each location at the sample plane. We always used holographic spots of 10 μm to photostimulate neurons, corresponding to an axial resolution of 9 μm at the center and < 14 μm at the edges of the FOV, respectively (**Supplementary Fig. 4C**).

We photostimulated ChRmine expressing cells (**Supplementary Fig. 4D**) with a low repetition rate laser (10 MHz, 1030 nm, 150 fs) by using 10 μm holographic spots and sending a train of 10 pulses of 20 ms in duration at a frequency of 4.2 Hz with a power (measured at the GRIN lens output) of 30-40 mW at the center of the FOV (**Supplementary Fig. 4E**), which was smoothly increased for off-center spots until reaching 60-80 mW at the edges of the FOV, to compensate for the GRIN lens aberrations.

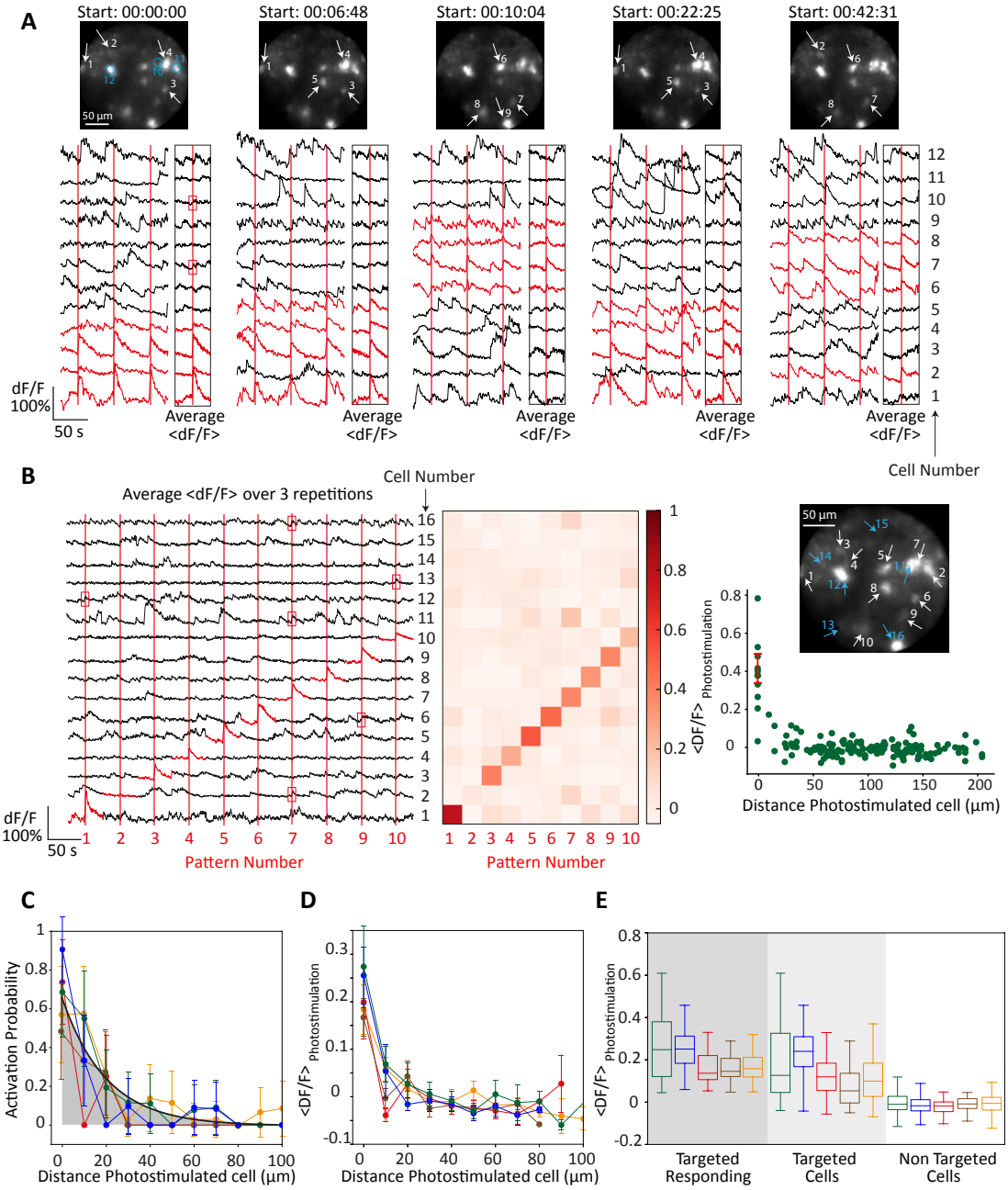

Figure 6. High resolution photostimulation in freely moving mice. A. Photostimulation of different groups of 4 neurons. Photostimulated neurons are indicated by arrows in the different z projections of each acquisition, and their calcium traces are plotted in red. For each group of neurons, the photostimulation was repeated 3 times, and the average signal was calculated and plotted as "Average <dF/F>". The starting time of each experiment relatively to the first acquisition is indicated on the top. B. Photostimulation of 10 different neurons, one by one. Left: Average <dF/F> traces over 3 photostimulation repetitions for every neuron. Traces of neurons photostimulated are plotted in red. Red frames highlight instances of increased activity for non-targeted neurons concomitant with the photostimulation period. Middle: heat map representing the average

fluorescence change $\langle dF/F \rangle_{Photostim}$ upon photostimulation for photostimulated neurons (1-10) and control neurons (11-16) for each photostimulation pattern. Right: z-projection of the FOV showing targeted (white arrows) and non-targeted (blue arrows) neurons. Plot of $\langle dF/F \rangle_{Photostim}$ for each neuron as a function of the distance from the photostimulated cell. All example data are taken from one FOV in animal #2, see Supplementary Table 1. C-E. Population analysis of the photostimulation efficiency on 5 different FOVs and 3 different mice. Each color corresponds to a different FOV. C. Activation probability of neurons as a function of the distance from the photostimulated cells. The black solid line is a fit with an exponential decay, the gray region refers to the area underneath the fit. D. $\langle DF/F \rangle_{Photostim}$ for neurons that show a positive response to the photostimulation as a function of the distance from the photostimulated cells. In C and D in the case of multi-target photostimulation, we considered the distance from the closest photostimulated cell. E. Average $\langle DF/F \rangle_{Photostim}$ for targeted and responding; targeted (both responding and non-responding); and non-targeted neurons, showing a significant difference in the response for targeted and non-targeted neurons. See the main text and Methods, for a detailed explanation of how $\langle DF/F \rangle_{Photostim}$ and the activation probability were calculated. Data are taken from one FOV in animals #2/3/4, see Supplementary Table 1. Power distribution correction and photostimulation paradigm are detailed in see Supplementary Figure 4. Acquisition examples are presented in Suppl. Video 3.

Fig. 6A, B show representative traces of one FOV in which we sequentially photostimulated different groups of neurons (**Fig. 6A and Supp. Video 3**) or individual neurons one by one (**Fig. 6B**). We repeated each photostimulation pattern for three consecutive times, with an interval of 50 s, as shown in the DF/F traces of **Fig. 6A**. To quantify the response of targeted cells to photostimulation, we averaged the DF/F signal over the three consecutive repetitions, generating the average <DF/F> shown in the rectangular boxes of **Fig. 6a** (in **Fig. 6B** we only show the average <DF/F> traces). As explained in the **Methods**, we used <DF/F> to compare the mean signal 2s before $\langle DF/F \rangle_{Before}$ and after $\langle DF/F \rangle_{After}$ photostimulation to assess if a neuron was or not photo-activated and to calculate the induced increase of fluorescence signal $\langle DF/F \rangle_{Photostim} = \langle DF/F \rangle_{After} - \langle DF/F \rangle_{Before}$ in response to photostimulation. A neuron was considered photostimulated if $\langle DF/F \rangle_{Photostim}$ was greater than 3 times the standard deviation of the baseline signal.

As shown in the traces of **Fig. 6A, B** we were able to selectively photo-activate only the neurons of interest, inducing responses on average of $\langle DF/F \rangle_{Photostim} \approx 25\%$, with very little cross activation of non-targeted cells (marked with red rectangles on the average traces). As a proof of the stability of the system, in **Fig. 6A** we also indicate the starting time of each acquisition with respect to the first one. As also shown in **Fig. 5**, we could reliably perform imaging and photostimulation experiments on the same FOV for hours (see also **Supplementary Video 2**).

As quantified in the population graphs of **Fig. 6 C, D**, (representing the average behavior over 50 different photostimulation sequences, 5 different days of measurement on 3 mice) cross activation of non-targeted cells was only visible at distances < 30 μm from one of the targeted cells, after which the activation probability and the $\langle DF/F \rangle_{Photostim}$ decayed to zero. The ensemble of data in **Fig. 6C** could be fitted with a single exponential decay function A*exp(-x/k), with x vector of distances from the photostimulated cells, A normalization factor, k=20±5 μm characteristic decay distance, confirming the high spatial selectivity of the photostimulation experiments. Overall, these results demonstrate that 2P-FENDO has enough sensitivity and it is sufficiently robust to allow cell selective photostimulation in freely moving animals.

Discussion

We have developed a novel fiber-based microscope, named 2P-FENDO for the 2P all-optical control and high-speed imaging of neuronal activity in head-fixed and freely moving mice with cellular resolution. This was demonstrated using 2P holographic photostimulation and 2P imaging in the cortex (L1, L2/3) of mice injected with the opsin ChRmine and/or the calcium indicator jGCaMP7s.

We have used 10-20 μm diameter imaging and 10 μm diameter photostimulation spots, which enabled increasing the total photon flux while keeping the power per core below the threshold for self-phase modulation (≈10 mW for 80 MHz repetition rate lasers [31–35]) (**STAR Methods**). We have demonstrated that the inter-core delay dispersion properties of the fiber bundle efficiently decouple the 2P excitation from different cores, thereby maintaining

axially confined (< 8 μm at the center of the FOV, < 14 μm at the edges) excitations almost independently of the lateral spot size. When illuminating multiple cores simultaneously, the pulses from each core reach the output fiber facet at slightly different times. The GRIN lens is then used to re-image the output facet at the sample plane. In practice, at any given time, even if multiple cores are excited together at the fiber entrance, only one focus appear at the sample plane, as all the other cores are delayed differently (within few ps) by the fiber bundle. The fiber bundles used here thus behave as temporal multiplexing devices, similar to previously investigated systems used for imaging[46–48], with the notable difference that the number of multiplexed points in this case can be as large as the number of cores in the bundle (~ 15000), as opposed to the < 100 of previous works.

By using this illumination approach combined with a high detection efficiency EM-CCD camera, we have demonstrated up to 50 Hz functional imaging capability on a FOV of 250 μm in diameter (see **STAR Methods** for possible strategies to enlarge further the FOV), which represents to our knowledge the fastest acquisition speed so far demonstrated in 2P fiber-bundle microscopes. Even at the highest acquisition speed, the total power sent to the sample (**STAR Methods**) was always kept well below the reported illumination threshold (≈250 mW) for persistent measurable brain damage[49]. Higher acquisition speeds with sufficient SNR could be reached by adapting the scanning strategy, for instance by scanning only on the cells of interest, such as in random access microscopy [50], or by using the unique capability of 2P-FENDO to generate static holographic spots.

We have demonstrated single and multi-target 2P photostimulation using holographic spots of 10 μm and an average power per cell of 30-80 mW. Considering the losses through the fiber and the need to compensate for aberrations of the GRIN lens, with the current laser (10 MHz; 1030 nm, 5W) we could photostimulate ~ 10 neurons simultaneously, a number that could be easily increased by using commercially available higher power (up to 60 W) and lower repetition rate (< 1 MHz) lasers.

Previous studies[6,7,9,51–55] have shown that small cortical subnetworks (<30 neurons) distributed on FOVs comparable in size with what is currently reachable through 2P-FENDO, can encode for perception, or bias learned

behavioural tasks. It was also shown that the manipulation of few highly connected "*hub*" cells can control the synchronicity of larger neuronal networks [6,55]. We therefore anticipate that 2P-FENDO, will enable to similarly affect behavioural outputs through the manipulation of defined microcircuits.

Over conventional 1P miniscopes[11,13,20,28], 2P-FENDO shows superior axial resolution and thus *z* sectioning capabilities and larger penetration depth. Multiphoton miniaturized microscopes based on the use of a single optical fiber and a miniaturized scanner unit[15,19,26,27] offer higher spatial resolution and thus superior imaging quality, mainly because the lateral resolution is not limited by the inter-core spacing as in fiber bundles. Compared to these systems, 2P-FENDO uses a larger illumination spot with no cost in the axial resolution, enabling 50 Hz imaging acquisitions albeit with the lower imaging resolution imposed by the fiber bundle. Compared to previously demonstrated fiber bundle based 2P microscopes [18], 2P-FENDO has a much higher acquisition speed and uses smaller and implantable probes. With respect to all these systems, 2P-FENDO is the only technology today capable of cell-precise multitarget 2P photostimulation in freely moving animals, which greatly increases the spectrum of applications within the reach of flexible microendoscopes. With respect to our previously demonstrated 1P fiber bundle system[16], 2P-FENDO presents all the advantages of 2P excitation, a higher acquisition speed and the use of a smaller GRIN lens, suitable for deep implants.

A major advantage of 2P-FENDO is the simplicity of its implementation. For imaging it only requires minor modifications of a standard 2P imaging system (larger imaging spot and camera detection), without the need of miniaturized scanning units and complex custom made optical architectures, which are typical of 2P miniaturized microscopes [15,19,26,27]. Furthermore, considering that good axial resolution is obtained thanks to the ICDD effect of the fiber, 2P-FENDO does not require additional techniques, such as temporal focusing [56], to maintain axial resolution for extended holographic spots. This will also enable to use of the same microscope for head restrained and freely moving experiments.

Contrary to previous works[45,57,58] performed in standard 2P microscopes, in which we used SLMs to create multiple 2P excitations distributed in three dimensions, working with a fiber bundle prevents the SLM from axially shifting

the generated patterns. As a result, in this configuration the SLM can only be used to target neurons located at one focal plane, which coincides with the imaging plane. By adding an axially shifting device, such as a tunable lens[18,27] or a step motor[59] after the fiber, one could simultaneously shift the imaging and photostimulation planes. By imaging at 20 Hz per plane, this could enable the subsequent acquisition of ~5 different planes at the total speed of 4 Hz. However, adding more optical components (such as tunable lenses) would also increase the complexity, volume and weight of the resulting device.

Camera detection strategies, combined with multipoint illumination, were demonstrated to be able to detect fluorescence signal down to 300 μm in brain tissue [60,61], after which the images become too blurred because of scattering effects. In this manuscript we have demonstrated imaging until depths of about 200 μm, limited by the working distances of the GRIN lens. Optimization of surgical techniques and miniaturization of implants represent further developments of endoscopic technologies for investigation of neuronal circuits located deep in the brain. Combined with GRIN lens brain implantation strategies, 2P-FENDO can be employed to investigate functions of selected neurons in brain regions unreachable by multiphoton microscopy such as the hypothalamus[62], the amygdala neuronal circuits [63], or the thalamus [64]. For this, both GRIN lenses used in here (see **Table 1**) have a total diameter of 1.3 mm, which is comparable to previously implanted GRIN lenses [51,65,66].

When performing photostimulation experiments in freely moving animals, the stability of the implant is of great importance to reliably photostimulate the targeted cells. We have demonstrated an average displacement of the FOV, of around 2 μm during acquisitions of 300s, smaller than the size of a cell, and a long-term stability of the implant. However, we have also observed movements of the FOV larger than 5 μm, even if for short periods of time. For repetitive photostimulations, this limitation could be overcome with the implementation of an active feedback loop that registers in real time the movement of the FOV and corrects the phase on the SLM to recenter the photostimulation pattern.

2P holographic photostimulation, combined with adequate optogenetic tools[67], makes it possible to selectively activate or inhibit specific neurons or discrete

networks within a larger population, even among a molecularly indistinguishable sub-type. This ability, together with that of precisely controlling the spike timing, is fundamental to probe possible causal links between perception, neuronal activity and behaviour, which are hard to understand with functional imaging alone[1,3,9]. Probing the role of spike timing and synchronicity in specific networks (e.g., in the visual cortex for sensory perception), or driving a specific temporal activity in relevant subgroups of neurons to trigger an appropriate behavioral response, are challenges that can be addressed with a 2P holographic photostimulation system[68]. Yet, most experiments exploring neuronal network activity are performed in head-fixed conditions, tempering the impact of animal free motion on neuronal processing. Recent works[69,70] showed for example that three-dimensional head motion modulates visual integration in primary visual cortex V1. The heterogeneity in directionality and timing of single cell responses in V1 resulting from head motion uncovered a multitude of network dynamics that cannot be observed in head fixed conditions. With the capability to simultaneously image and control neuronal activity with single-cell resolution in freely moving animals, 2P-FENDO will enable to identify and challenge these emerging networks dynamics in order to unravel the complex brain processes hidden behind naturalistic behaviour.

Acknowledgments

We acknowledge support from the IHU FOReSIGHT grant (Grant P-ALLOP3-IHU-000), the Fondation Bettencourt Schueller (Prix Coups d'élan pour la recherche française), the Axa research funding the 'Agence National de la Recherche' (grants ANR 19-CE19-0001-01, 2MEnHoloMD) the Human Frontiers Science Program (Grant RGP0015/2016), Imagine Nano, the ERC advanced Grant HOLOVIS (ERC-2019-AdG; Award no. 885090), the ERC Horizon 2020 H2020-ICT (DEEPER, 101016787), Israel Science Foundation (1361/18), Israeli Ministry of Science and Technology (Grant 712845). We would like to thank Serge Charpak, Marine Tournissac and Manon Omnès (Vision Institute, Paris) for helpful discussions and pilot imaging experiments, Andrea Giovannucci for help with CaImAn, Aaron Benson Wong (ErasmusMC Rotterdam) for help in calcium imaging data analysis, Vincent de Sars for WaveFront IV software development, and Manuel Simonutti,

Julie Degardin and Quenol Cesar from the animal facility of the Institut de la vision, for their help and support on animal experimentation.

Declaration of interest

The authors declare that they have no known competing financial interests or personal relationships that could have appeared to influence the work reported in this paper.

Author Contributions

N.A., A.L.C. and C.T. built the optical setup. N.A. and A.L.C. developed the acquisition software and performed the optical characterization. O.K. conceived the experiment for measuring the inter core delay dispersion. N.B. measured and analysed the inter core delay dispersion. F.G.C.B. and C.T. designed and developed the implant for freely moving experiments. F.G.C.B., V.Z. and F.B. developed the surgical procedures and performed viral injections. V.Z. and F.B. acquired in vivo and in vitro z-stacks and preliminary calcium imaging data in vivo. F.G.C.B. and A.L.C. performed imaging and photostimulation experiments in freely moving mice. N.A., F.G.C.B. and A.L.C. analysed the data. N.A., F.G.C.B. and V.E. wrote the paper with the contribution of all the authors. N.A. and V.E. conceived and supervised the project.

STAR Methods

Key Resources Table

REAGENT or RESOURCE	SOURCE	IDENTIFIER
Bacterial and virus strains		
AAV9-CMV-GFP-WPRE	Xiong *et al* J Clin Invest. 2015	Addgene Cat#67634
AAV1.CAG.tdTomato	Edward Boyden lab	Addgene Cat#59462-AAV1
AAV9-syn-jGCaMP7s-WPRE	Dana *et al* Nat Methods. 2019	Addgene Cat#104487-AAV9
AAV1-hSyn-ChRmine-mscarlet-Kv2.1-WPRE	Marshel *et al* Science. 2019	Addgene Cat#130995
Chemicals, peptides, and recombinant proteins		

Dexazone (Dexamethasone) - Virbac	Centravet	Cat#DEX216
Laocaine (Lidocaine) - MSD	Centravet	Cat#LAO001
Rompun 2% (Xylazine) - Bayer	Centravet	Cat#ROM001
Ketamidor (Ketamine) - Axience	Axience Santé Animale	Cat#152500
Lubrithal (Eye gel) - Dechra	Centravet	Cat#LUB001
Buprenorphine	Axience Santé Animale	Cat#151244
Isoflurane	Axience Santé Animale	Cat#153613
Antisedan-ANTIDORM	Axience Santé Animale	Cat#152494
Tetric Evoflow A1-IVOCLAR	Dentaltix	Ca#45TE595953
Experimental models: Organisms/strains		
C57BL/6J	Janvier Labs	https://janvier-labs.com/fiche_produit/2-c57bl-6jrj/
Software and algorithms		
WaveFront IV	Emiliani's Lab	Available from: vincent.de-sars@inserm.fr
MATLAB 2020b	Mathworks	https://www.mathworks.com/
FIJI/ImajeJ 2.0.0	ImageJ	https://imagej.net/software/fiji/
LabView 2016	National Instruments	https://www.ni.com/fr-fr/shop/labview.html
DeepLabCut 2.1	Mathis's Lab (Mathis et al. 2018)	https://github.com/DeepLabCut/DeepLabCut
CaImAn 1.9.7	Flatiron Institute	https://github.com/flatironinstitute/CaImAn
Other		
Laser Spark Alcor - ALCOR 920-4	Spark Alcor	https://spark-lasers.com/produit/alcor/
EM-CCD Camera iXon Ultra 888	Andor - Oxford Instruments	https://andor.oxinst.com/products/ixon-emccd-cameras-for-physical-science

Laser Goji	Amplitude	https://amplitude-laser.com/products/femtosecond-lasers/goji/
LCOS-SLM X10468-07	Hamamatsu	http://www.hamamatsu.com.cn/UserFiles/DownFile/Product/20130920095320007.pdf
Image Fiber FIGH-15-600N	Fujikura	https://www.fujikura.co.jp/eng/products/optical/appliedoptics/03/2050110_12902.html
GRIN Lens 1: GT-MO-070-016-ACR-VISNIR-30-20	Grintech	https://www.grintech.de/fileadmin/user_upload/Datenblaetter/High-NA_chromatic_and_field_corrected_Endomicroscopic_Imaging_Objectives.pdf
GRIN Lens 2: GT-MO-080-032-ACR-VISNIR-08CG-20	Grintech	https://www.grintech.de/fileadmin/user_upload/Datenblaetter/High-NA_chromatic_and_field_corrected_Endomicroscopic_Imaging_Objectives.pdf

RESOURCE AVAILABILITY

Lead contact

Extended information and requests for resources should be directed to the lead contact, Dr. Valentina Emiliani (valentina.emiliani@inserm.fr).

Materials availability

This study did not generate new unique reagents, mouse lines or optical elements. Commercially available resources are indicated in the key resources table.

Data and Code Availability

• All data reported in this paper will be shared by the lead contact upon request.

• This paper does not report original code.

• Any additional information required to reanalyze the data reported in this paper is available from the lead contact upon request.

Experimental model and subject details

Mouse lines and knockout genetics

Wild-type males and females C57BL/6J mice (Janvier Labs) were used for experiments. All experiments were performed in accordance with EU Directive 2010/63. The protocols were reviewed by the local animal experimentation ethics committee (CETEA n.44) and authorized by the French Ministery of Research and Education (#201803261541580). Advices on procedures, refinement of animal experimentation standards, and pain and distress management are provided by the Local Animal Welfare Office. Animals are housed in 2-5 per cage, with a light-dark cycle of 12+12 hours, and food and water ad libitum.

METHOD DETAILS

Imaging setup

The imaging laser was an ultrafast fiber laser (Spark Alcor, central wavelength of 920 nm, pulse duration of 150 fs, total power of 4 W, repetition rate of 80 MHz), whose output power was controlled by using a lambda half waveplate and a polarizing beam splitter. The internal laser compressor was set to ~ - 90000 fs^2 to compensate for the fiber dispersion. The laser beam was first magnified using a 5X beam expander. It was then sent through a motorized iris to control the size of the beam at the fiber (and therefore at the sample), in this way we could control the imaging power by changing the imaging spot size without effective changes in the power/core. This enabled to keep the power per core always lower than the onset of self-phase modulations effects (~10 mW/core). The galvo-resonant mirrors were placed in a Fourier plane of both the iris and the fiber entrance. The beam passing through the motorized iris was focused at the entrance of the galvo-resonant mirrors using 3 lenses (f1=200 mm, f2=60 mm, f3=500 mm, for

simplicity in the scheme of the setup in Fig.1 only one lens between the first iris and the galvo-resonant mirrors is shown). After the galvo-resonant mirrors, a first lens (f4=400 mm) created an intermediate imaging plane where we placed a second iris that was perfectly imaged at the fiber entrance using one lens (f5=200 mm) and a microscope objective (Olympus, UPLFLN 10X, 0.3 NA). The second iris prevented the beam to be scanned outside of the fiber region, thus avoiding unwanted thermal and nonlinear effects that might come from the fiber coating or the fiber holder. The average power measured after the second iris was ~ 50% of the power measured before. This is because, to uniformly illuminate the fiber entrance, the second iris cut the outer parts of the scanned regions, where galvo and resonant scanners decrease their speeds and spend more time. The fluorescence emission from the sample was collected through the endoscope and the same 10X microscope objective. A long pass dichroic beam splitter was then used to separate it from the incoming laser beam and reflect it to the EM-CCD camera (Andor Ultra 888, 1024x1024 pixels, pixel size 13.3x13.3 μm^2). The camera was used in crop mode with a sub array of 512x512 pixels corresponding to a maximum frame rate of 94 fps. A 180 mm focal length lens was used to focus the fluorescence onto the camera after passing through 2 IR blocking filters (Thorlabs TF1). To select green (for GFP and GCaMP7) or red (for TdTomato) fluoresce emission, a flip motor (Thorlabs MFF102) switched from a green to a red emission filter.

Photostimulation setup

The photostimulation laser was a low repetition rate fiber laser (Goji, central wavelength of 1040 nm, pulse duration of 150 fs, total power of 5 W, repetition rate of 10 MHz, internal laser compressor set to ~ - 90000 fs^2) whose power was controlled by a lambda half waveplate and a polarizing beam splitter. The laser beam was magnified by a 5X beam expander and spatially shaped by an SLM (LCOS-SLM X10468-07, Hamamatsu Photonics, resolution 800 × 600 pixels, 20 μm pixel size). Two lenses ($f1_{SLM}$=250 mm and $f2_{SLM}$=300 mm) conjugated the SLM plane with the entrance of the microscope objective (Olympus, UPLFLN 10X, 0.3 NA). A short pass dichroic mirror was used to recombine the

photostimulation and imaging beams before entering the microscope objective. The laser beam was made slightly divergent with the beam expander before arriving to the SLM, which applied a defocus to the beam to compensate the divergence. In this way we separated in z the planes of the 0th and 1st diffraction order of the SLM. A small beam blocker was then used to block the 0th order (see Ref.[71]).

Fiber and GRIN lens specifications

The fiber bundle used in the experiments was a 2 meter commercially available bundle (Fujikura model FIGH-15-600N), which was coupled to chromatic and field corrected GRIN micro-objectives (Grintech models GT-MO-080-032-ACR-VISNIR-08CG-20 or GT-MO-070-016-ACR-VISNIR-30-20, diameter of 1.3 mm). The chromatic correction allows both the fluorescence and two laser wavelengths, for imaging and photostimulation, to be focused on the same plane.

The diameter of the FOV (D_{FOV}) currently accessible to 2P-FENDO is limited by the diameter of the optical fiber bundle (D_{Bundle}) and the magnification of the GRIN lenses (M_{GRIN}), according to the relation $D_{FOV} = D_{Bundle}/M_{GRIN}$. At the same time, the lateral resolution (d_{xy}) is limited by the intercore distance within the fiber bundle ($d_{intercore} \approx 4.5\ \mu m$ in for the current fiber bundle) and M_{GRIN}, according to $d_{xy} = d_{intercore}/M_{GRIN}$. To enlarge the FOV without affecting the lateral resolution of the system, one could use a bundle with a larger diameter, matching the GRIN lens diameter (~1 mm). Similar bundles are commercially available but have a reduced flexibility with respect to the ones used in this work, which would restrain too much the movements of the mice. The only alternative could be to reduce the magnification of the GRIN lens, which in turns depends on the ration between the NA on the sample side and that on the fiber side according to $M_{GRIN} = NA_{sample}/NA_{fiber}$. Reducing the NA on the sample side could therefore enlarge the FOV at the expenses of the detected fluorescence signal. Additionally, a lower NA could be obtained with a GRIN lens of a smaller diameter (GRIN lenses with a diameter as small as 300 μm are already commercially available with NAs of 0.5), which might be beneficial to reduce further the size of the endoscope. However, reducing the GRIN lens magnification would also cause

a decrease in the lateral resolution. To compensate for this, one might use fiber bundles with more closely spaced cores, which are already commercially available (such as the S series from Fujikura).

GRIN lens 2 is designed to be at a distance, d=200 μm from the fiber bundle, and to produce a working distance, WD, of 80 μm (in water or brain tissue) below a cover glass of 170 μm in thickness (see **Table 1** in the main manuscript). To increase this value and reach deeper cortical layer (L2/3), we have proceeded as follows: 1) we kept the GRIN lens always in contact with the fiber bundle, which increased the working distance in brain tissue of ~ 70 μm; 2) we used cover glasses of thickness of ~ 100 μm, which further increased the working distance of ~ 60 μm, taking into account the refractive index mismatch between glass and water (or brain). With these modifications, we could reach a working distance of ~ 150 to 200 μm below the cover glass for in vivo experiments in the water immersion configuration (see **Supplementary Fig. 3**). GRIN lens 2 is specified by the manufacturer (Grintech) to work in water (or brain tissue) after the protective cover glass. To keep as much as possible these ideal conditions, in all the experiments on rhodamine, fixed brain slices, pollen grains, head-fixed animals the space between the GRIN lens and the cover glass was filled with water. To prevent water evaporation, experiments in freely moving mice, in which the GRIN lens is cemented on top of the craniotomy for several days, the space between the GRIN lens and the cover glass was filled with a drop of index matching oil for microscope objectives. This, as shown in Ref.[72,73] has the effect of shifting the effective focal plane, as better quantified in **Supplementary Fig. 3**. In the oil immersion configuration, the maximum attainable working distance is lower, namely ~ 120 to 160 μm.

For the characterization and the head-fixed experiments the fiber and GRIN lens were held on two separated mounts and could be moved one respect to the other by using a three-dimensional translation stage.

Power measurements

Because of the filling factor of the fiber bundle (~ 50% transmission when using a large spot encompassing multiple cores), the infra-red transmission of the low

NA objective (~80% at 920 nm and ~60% at 1030 nm) used to focus the laser inside the fiber and the coupling between the GRIN lens and the fiber bundle (~90% efficiency), the total transmission for the imaging laser is ~ 35% and for the photostimulation laser is ~ 27%. This value can be increased by using a higher transmission lens in the infra-red range but will still be ultimately limited by the filling factor of the fiber bundle.

For the photostimulation laser one additionally has to account for the 70% efficiency of the SLM (considering reflection efficiency, zero order losses, diffraction efficiency losses), and the transmission of polarization optics (lambda half waveplates and polarizers to control the power, beam expander to enlarge the beam at the SLM, additional lenses to get to the objective pupil). Considering all this, we measured a total available photostimulation power after the endoscope of 600 mW, when starting with a 5 W laser.

Because the imaging spot is scanned at the fiber entrance by using a galvo-resonant scanner, in order to completely fill the fiber we scanned the laser beam on a square of lateral dimension of ~ 600 μm, where the diameter of the fiber bundle is ~ 550 μm. This ensures uniform illumination of the fiber bundle. In order to prevent the laser beam to hit the fiber cladding, which could possibly damage the fiber, we clipped the beam by using an iris placed in the first image plane after the scanners. Because the resonant scanner passes more time on the edges, in which it slows down and turns around, than in the center, a large amount of the total power is lost on the iris (or, if an iris were not used, it would be lost outside of the fiber). In our system, the average power measured after the GRIN lens while scanning the entire FOV was 50% of the power measured when the beam was static (not scanned) at the fiber entrance.

Signal comparison between core-by-core scanning and multi-core illumination.

A key property of 2P-FENDO, which enables faster acquisition speeds with respect to previous 2P fiber bundle approaches is the optimized illumination and detection scheme. By making an extended excitation spot, and detecting the 2P fluorescence with a high quantum efficiency and low readout noise EMCCD

camera, 2P-FENDO gains in the total amount of photons detected per cell, which is ultimately the signal one is interested in when performing calcium imaging. Let us consider the case of a fiber bundle with a filling factor of 50% (F=0.5) and compare the two-photon signal (2PS) coming from a cell that occupies N=20 cores of the fiber bundle in two different cases: 1) The scanning microscope configuration, in which a laser intensity I is focused on a diffraction limited spot that is scanned on the cell on a total time T. Each core is thus illuminated for a total time that is T/(N/F) = T/(2N) in the case of a 50% filling factor. This is because the scanning beam at the fiber entrance has to scan also on the dark space in between different cores. The detection is performed with a PMT that has a quantum efficiency of ~ 40%. To avoid damage of the fiber, which mainly happens because during scanning one also scans in the space between fiber cores, the scanning configuration is practically limited to power values < 100 mW; 2) The 2P-FENDO configuration in which every core is excited simultaneously for a total time T with the same intensity Imax, just below the threshold for self-phase modulation (SPM) to occur, which was measured to be roughly 10 mW per core[1–4]. The detection is performed with an EMCCD camera that has a quantum efficiency of ~ 90 %. For simplicity we will assume a twice higher quantum efficiency for the camera than for the PMT. In the ideal case, in which the 2PS scales quadratically with the laser intensity, we obtain:

$$2PS_{Scan}^{Ideal} \propto A\, I^2\, T\, F = A\, I^2 \frac{T}{2}$$

$$2PS_{FENDO}^{Ideal} \propto I_{max}^2 T\, N$$

Where we have introduced a scaling factor A representing the ratio between the quantum efficiency of the PMT and the camera (A=0.5 in this case).

However, when using small core fibers or fiber bundles, SPM results in a longer pulse at the fiber output. This, in turns, means that the quadratic relation between the 2P signal and the excitation power breaks down above 10 mW, and the 2P signal grows sub-optimally, eventually only scaling linearly as the power is further increased (see for instance Ref.[18,32,34,35]). For instance, from Ref.[35], a laser pulse of 150 fs at the fiber output for a power of 10 mW becomes ~ 1 ps when the

power is increased to 100 mW. If we call S_core (I) the 2PS from a single core of the fiber bundle as a function of the laser intensity, we can write the previous equations as

$$2PS_{Scan} = A\, S_{core}(I)\, T\, F$$

$$2PS_{FENDO} = S_{core}(I = I_{max})\, T\, N$$

If we limit to powers per cores < 100 mW, considering that Score(I=100mW) ≈ 15∗Score(I=Imax=10mW), 2P-FENDO, thanks to the wider illumination and the higher camera quantum efficiency is able to detect 2.5 or 5 times the signal when using N=10 or N=20 cores and total power of 100 mW or 200 mW. This ultimately allows 2P-FENDO to increase proportionally the acquisition speed with respect to 2P scanning techniques when using comparable laser powers

Controlling software and synchronization with photostimulation.

A custom-designed software written in LabVIEW was used to control the motorized iris at the imaging laser, the galvo-resonant scanners, the photostimulation laser power, the fast shutter to control the photostimualtion timing, the z step motor used to move vertically the micro-endoscope, and the XY position stage that moved the anesthetized mouse with respect to the endoscope.

A custom-designed software, Wavefront-Designer IV, written in C++ and using the open graphic library Qt 4.8.7, controlled the SLM for the dynamic CGH configuration, using Gerchberg–Saxton-based algorithms. The software also included the phase corrections for the first-order Zernike aberrations.

The EM-CCD camera was controlled with its software (Andor Solis) and externally synchronized with the LabVIEW software for z-stack and photostimulation experiments.

During photostimulation a fast shutter was used to let through the Goji laser for 10 ms every 140 or 225 ms. The EM-CCD camera was used in external exposure mode and turned off between 25 to 40 ms in correspondence to the periods of Goji illumination. With this we removed completely any artifact that might come from the direct excitation of fluorescence from the photostimulation laser. For a better visualization of the photstimulation protocol, see **Supplementary Fig. 4**

Viral vectors injections and surgical procedure for in-vivo experiments.

Stereotaxic injections were performed to deliver high titer adeno-associated viral vectors to cortical neurons of 5-8-weeks-old mice for expression of GFP, TdTomato, the calcium reporter jGCaMP7s, the opsins ChRmine, or jGCaMP7s+ChRmine. The following viral constructs were used (viral concentration in the order of 10^12 vp/ml): AAV9-CMV-GFP-WPRE (Vision Institute vector core facility, Paris), AAV1.CAG.tdTomato (Addgene), AAV9-syn-jGCaMP7s-WPRE (Addgene), AAV1-hSyn-ChRmine-mscarlet-Kv2.1-WPRE (plasmid from Addgene), or a mixture 2:1 of AAV9-syn-jGCaMP7s-WPRE + AAV1-hSyn-ChRmine-mscarlet-Kv2.1-WPRE. Imaging and photostimulation experiments were performed 3-15 weeks after injection. All surgical procedures were performed in sterile conditions on mice anesthetized with intraperitoneal injection of a mixture of ketamine (60-80 mg/Kg) - xylazine (5-8 mg/Kg). Eyes were protected with ophthalmic gel, and the animal was placed on the stereotaxic frame. The anti-inflammatory dexamethasone sodium phosphate (0.01 mg/g) and analgesic buprenorphine (0.1mg/Kg) were injected subcutaneously before surgery. Lidocaïne 2% was injected subcutaneously before opening the skin. Body temperature was kept constant at 37°C and anesthesia parameters were monitored all along the experiments (homeothermic system, Kent Scientific). Subcutaneous injections of 0.1 ml sterile saline solution ensured rehydration all along the experiments.

For viral vectors injections, a craniotomy of 0.5-0.7 mm was made on the skull overlying V1 or wS1 cortex, and 1µl solution containing the viral vector was delivered at 150-50 µm depth from the brain surface. Skin was sutured and mouse recovered from anesthesia. Buprenorphine was injected 8-12 hours after surgery.

The cranial window surgery was performed 3-15 weeks after injection. A cranial window of 3-3.5 mm was made above and centered on the viral injection site. Dura was removed while keeping the brain surface moist with sterile saline solution. A 3 mm cover glass (#0, 0.085 to 0.13 mm thickness; Multichannel

System) was placed on top of the craniotomy and sealed with dental cement (Tetric EvoFlow A2, Ivoclar). The head plate was then fixed with dental cement.

Mice were given at least 3 days to recover from the cranial window surgery done under ketamine/xylazine. On experimental day one, mice were maintained head-fixed under isoflurane anesthesia (<1.5%) for 40min. The region with best expression of opsin and calcium reporter was identified under 2P FENDO. Then the fiber/GRIN lens holder was fixed with dental cement over the window.

For *in vivo* freely moving imaging and photostimulation experiments, mice were let recover in their home cage. The light and short isoflurane anesthesia allowed for fast recovery, in the order of minutes. At the end of the recording session (3-4h) mice were put back on isoflurane (<5 min) to remove the fiber from the holder. At the start of every following session, mice were maintained 20 min head-fixed under isoflurane anesthesia to set-up the fiber back in the holder. With this holder system and cranial window surgical methodology, animals were recorded for successive experiments for up to 1.5 months. The only limitation being the growth of fibrotic tissue commonly observed in chronic windows that will end up blocking optical access.

Axial resolution measurements

For characterizing the axial resolution and performances of the 2P-FENDO, both for the imaging and photostimulation lasers, the 2P fluorescence from a thin (~1 μm) spin-coated fluorescent layer of rhodamine-6G in polymethyl methacrylate 2% w/v in chloroform was collected through the endoscope and sent to the camera detector. By using a z-step motor (Thorlabs DDS100), the endoscope (fiber+ GRIN lens) was scanned over the desired *z* range to collect 3D stacks of images. We performed the analysis of the recorded stacks with MATLAB and ImageJ. The 2P fluorescence values were obtained by integrating the intensity of all the pixels in a circular area containing the (imaging or holographic) spot, for each plane of the recorded stack. Reported values for the axial confinement were the fit of the axial profile of the spots with a Lorentzian model and referred to the FWHM of the curves.

Motion correction and movement estimation

We used CaImAn[41] to quantify and correct for the motion of the FOV, by using patched non-rigid motion correction. We used patches of 30-60 μm. For each frame f in the acquisition and for each patch p, we thus obtained the x and y displacement of the FOV in μm, called $\mathrm{d}_x(f,p)$ and $\mathrm{d}_y(f,p)$, from which we calculated the total displacement, according to $d(f,p) = \sqrt{\mathrm{d}_y(f,p)^2 + \mathrm{d}_y(f,p)^2}$. We then averaged $d(f,p)$ over all patches to obtain a mean displacement for each frame, i.e. $\langle d(f)\rangle_p$. We did not consider patches at the corners of the images as they contained a significant number of pixels that corresponded to areas outside of the fiber bundle and therefore would remain static during acquisition.

By synchronizing calcium acquisition with the videos of the animals moving in the cages, we could then divide the frames according to the animal speed into two groups: f^+ and f^-, for mouse speeds greater or lower than 5cm/s. We then calculated the average and the standard deviation of the mean displacement over relevant frames $\langle d\rangle_{p,f^+}$ and $\langle d\rangle_{p,f^-}$, which are plotted in Fig.3f.

QUANTIFICATION AND STATISTICAL ANALYSIS

Calcium data analysis

After motion correction, we let CaImAn automatically detect active neurons. We confirmed that the detected regions of interest (ROIs) corresponded to actual cells by visually inspected the images and manually removing ROIs that did not match neurons. For each found neuron, we used the SNR value produced by CaImAn, according to the definition given in Ref.[41]. To calculate DF/F traces, we used the *detrend_df_f* function from CaImAn.

The algorithm was run with the following parameters, following the CaImAn conventions: gnb=1 (global background components); low thresholds: rval_lowest=0.3, SNR_lowest=0.5, cnn_lowest=0.3; high thresholds: rval_thr=0.8; min_SNR=2 to 2.5; cnn_thr= 0.8 to 0.9. A neuron has to exceed all the low thresholds and at least one high threshold to be accepted. Occasionally, after

manual inspection we added few cells with SNR<0.5. We briefly remind that *rval* measures the spatial footprint consistency of each found component; *SNR* is calculated from strong peaks of fluorescence in a trace and considering the baseline noise over the whole trace; the *cnn* based classification quantifies the resemblance of a component to a neuronal soma using a 4-layer convolutional neuronal network.

For photostimulation data we always repeated the same photostimulation patterns for three consecutive times. We then averaged the DF/F signal over the three consecutive repetitions, generating the average < DF/F >. We used this average signal to determine if a neuron was or not photostimulated and to calculate the induced increase of fluorescence signal $\langle DF/F \rangle_{Photostim} = \langle DF/F \rangle_{After} - \langle DF/F \rangle_{Before}$ in response to photostimulation. We compare the average signal 2s before photostimulation $\langle DF/F \rangle_{Before}$ (which constitutes our baseline signal) with the average signal during the 2s following the middle of the photostimulation period $\langle DF/F \rangle_{After}$. As the photostimulation was composed by 10 pulses, we calculated $\langle DF/F \rangle_{After}$ by averaging over 2s after the 5^{th} photostimulation pulse. A cell (either targeted or non-targeted) was considered photostimulated if $\langle DF/F \rangle_{Photostim}$ was greater than 3 times the standard deviation of the baseline signal.

Image treatment

A downside of using disordered bundles is that the transmission and dispersion properties of each core can be slightly different, which results in inhomogeneous 2P signals from different cores even when imaging uniform fluorescent samples. In the images presented here, a Gaussian blur function was used to smooth out the core-to-core differences. Alternatively, this is can be solved, as shown in Ref.[18], by mapping the spatial distribution of the 2P fluorescence on a homogeneous microscope fluorescence slide and correcting for the fiber induced inhomogeneities in post processing.

Tracking data processing

The tracking videos were first analyzed in DeepLabCut, which was trained to recognize the implant and the body center on the freely moving mice. The model

was trained with between 15-20 labeled datasets from different mice videos, with different tracking camera-mice cage positions and illumination conditions. From DeepLabCut we extracted the implant and body center part positions in pixels for each frame and a likelihood estimation (value between 0 and 1). We only considered the positions for which the likelihood was at least >0.9 (good confidence estimation). We considered the implant position as the head position of the mouse and the camera frame rate is 50Hz. To calculate the velocity on the mice we divided the distance of the implant between two adjacent frames by the time interval between these two frames (1/50Hz). The same calculation was done for the acceleration but in this case, we divided the velocity in two adjacent frames by the time interval.

References

1. O'Connor, D.H., Huber, D., and Svoboda, K. (2009). Reverse engineering the mouse brain. Nature *461*, 923–929. 10.1038/nature08539.
2. Emiliani, V., Cohen, A.E., Deisseroth, K., and Häusser, M. (2015). All-Optical Interrogation of Neural Circuits. The Journal of Neuroscience *35*, 13917–13926. 10.1523/JNEUROSCI.2916-15.2015.
3. Marshel, J.H., Kim, Y.S., Machado, T.A., Quirin, S., Benson, B., Kadmon, J., Raja, C., Chibukhchyan, A., Ramakrishnan, C., Inoue, M., et al. (2019). Cortical layer-specific critical dynamics triggering perception. Science (1979) *365*. 10.1126/science.aaw5202.
4. Packer, A.M., Russell, L.E., Dalgleish, H.W.P., and Häusser, M. (2015). Simultaneous all-optical manipulation and recording of neural circuit activity with cellular resolution in vivo. Nat Methods *12*, 140–146. 10.1038/nmeth.3217.
5. Rickgauer, J.P., Deisseroth, K., and Tank, D.W. (2014). Simultaneous cellular-resolution optical perturbation and imaging of place cell firing fields. Nat Neurosci *17*, 1816–1824. 10.1038/nn.3866.
6. Carrillo-Reid, L., Han, S., Yang, W., Akrouh, A., and Yuste, R. (2019). Controlling Visually Guided Behavior by Holographic Recalling of Cortical Ensembles. Cell *178*, 447-457.e5. 10.1016/j.cell.2019.05.045.
7. Gill, J. V., Lerman, G.M., Zhao, H., Stetler, B.J., Rinberg, D., and Shoham, S. (2020). Precise Holographic Manipulation of Olfactory Circuits Reveals Coding Features Determining Perceptual Detection. Neuron *108*, 382-393.e5. 10.1016/j.neuron.2020.07.034.
8. Chen, I.-W., Ronzitti, E., Lee, B.R., Daigle, T.L., Dalkara, D., Zeng, H., Emiliani, V., and Papagiakoumou, E. (2019). In vivo sub-millisecond two-photon optogenetics with temporally focused patterned light. The Journal of Neuroscience *39*, 1785–18. 10.1523/jneurosci.1785-18.2018.

9. Zhang, Z., Russell, L.E., Packer, A.M., Gauld, O.M., and Häusser, M. (2018). Closed-loop all-optical interrogation of neural circuits in vivo. Nat Methods *15*, 1037–1040. 10.1038/s41592-018-0183-z.
10. Chong, E., Moroni, M., Wilson, C., Shoham, S., Panzeri, S., and Rinberg, D. (2020). Manipulating synthetic optogenetic odors reveals the coding logic of olfactory perception. Science (1979) *368*. 10.1126/science.aba2357.
11. Aharoni, D., and Hoogland, T.M. (2019). Circuit investigations with open-source miniaturized microscopes: Past, present and future. Front Cell Neurosci *13*, 141. 10.3389/fncel.2019.00141.
12. Skocek, O., Nöbauer, T., Weilguny, L., Martínez Traub, F., Xia, C.N., Molodtsov, M.I., Grama, A., Yamagata, M., Aharoni, D., Cox, D.D., et al. (2018). High-speed volumetric imaging of neuronal activity in freely moving rodents. Nat Methods, 1–4. 10.1038/s41592-018-0008-0.
13. de Groot, A., van den Boom, B.J.G., van Genderen, R.M., Coppens, J., van Veldhuijzen, J., Bos, J., Hoedemaker, H., Negrello, M., Willuhn, I., De Zeeuw, C.I., et al. (2020). Ninscope, a versatile miniscope for multi-region circuit investigations. Elife *9*. 10.7554/eLife.49987.
14. Zong, W., Wu, R., Li, M., Hu, Y., Li, Y., Li, J., Rong, H., Wu, H., Xu, Y., Lu, Y., et al. (2017). Fast high-resolution miniature two-photon microscopy for brain imaging in freely behaving mice. Nat Methods *14*, 713–719. 10.1038/nmeth.4305.
15. Zong, W., Wu, R., Chen, S., Wu, J., Wang, H., Zhao, Z., Chen, G., Tu, R., Wu, D., Hu, Y., et al. (2021). Miniature two-photon microscopy for enlarged field-of-view, multi-plane and long-term brain imaging. Nat Methods *18*, 46–49. 10.1038/s41592-020-01024-z.
16. Szabo, V., Ventalon, C., De Sars, V., Bradley, J., and Emiliani, V. (2014). Spatially Selective Holographic Photoactivation and Functional Fluorescence Imaging in Freely Behaving Mice with a Fiberscope. Neuron *84*, 1157–1169.
17. Dussaux, C., Szabo, V., Chastagnier, Y., Fodor, J., Léger, J.F., Bourdieu, L., Perroy, J., and Ventalon, C. (2018). Fast confocal fluorescence imaging in freely behaving mice. Sci Rep *8*, 16262. 10.1038/s41598-018-34472-x.
18. Ozbay, B.N., Futia, G.L., Ma, M., Bright, V.M., Gopinath, J.T., Hughes, E.G., Restrepo, D., and Gibson, E.A. (2018). Three dimensional two-photon brain imaging in freely moving mice using a miniature fiber coupled microscope with active axial-scanning. Sci Rep *8*, 8108. 10.1038/s41598-018-26326-3.
19. Li, A., Guan, H., Park, H.-C., Yue, Y., Chen, D., Liang, W., Li, M.-J., Lu, H., and Li, X. (2021). Twist-free ultralight two-photon fiberscope enabling neuroimaging on freely rotating/walking mice. Optica *8*, 870. 10.1364/optica.422657.
20. Aharoni, D., Khakh, B.S., Silva, A.J., and Golshani, P. (2019). All the light that we can see: a new era in miniaturized microscopy. Nat Methods *16*, 11–13. 10.1038/s41592-018-0266-x.
21. Helmchen, F., Fee, M.S., Tank, D.W., and Denk, W. (2001). A miniature head-mounted two-photon microscope: High-resolution brain imaging in freely moving animals. Neuron *31*, 903–912. 10.1016/S0896-6273(01)00421-4.

22. Sawinski, J., Wallace, D.J., Greenberg, D.S., Grossmann, S., Denk, W., and Kerr, J.N.D. (2009). Visually evoked activity in cortical cells imaged in freely moving animals. Proc Natl Acad Sci U S A *106*, 19557–19562. 10.1073/pnas.0903680106.
23. Gu, M., Bao, H., and Kang, H. (2014). Fibre-optical microendoscopy. J Microsc *254*, 13–18. 10.1111/jmi.12119.
24. Lombardini, A., Mytskaniuk, V., Sivankutty, S., Andresen, E.R., Chen, X., Wenger, J., Fabert, M., Joly, N., Louradour, F., Kudlinski, A., et al. (2018). High-resolution multimodal flexible coherent Raman endoscope. Light Sci Appl *7*, 10. 10.1038/s41377-018-0003-3.
25. Park, H.-C., Guan, H., Li, A., Yue, Y., Li, M.-J., Lu, H., and Li, X. (2020). High-speed fiber-optic scanning nonlinear endomicroscopy for imaging neuron dynamicsin vivo. Opt Lett *45*, 3605. 10.1364/ol.396023.
26. Klioutchnikov, A., Wallace, D.J., Frosz, M.H., Zeltner, R., Sawinski, J., Pawlak, V., Voit, K.M., Russell, P.S.J., and Kerr, J.N.D. (2020). Three-photon head-mounted microscope for imaging deep cortical layers in freely moving rats. Nat Methods *17*, 509–513. 10.1038/s41592-020-0817-9.
27. Zong, W., Obenhaus, H.A., Skytøen, E.R., Eneqvist, H., de Jong, N.L., Vale, R., Jorge, M.R., Moser, M.-B., and Moser, E.I. (2022). Large-scale two-photon calcium imaging in freely moving mice. Cell *185*, 1240-1256.e30. 10.1016/j.cell.2022.02.017.
28. Stamatakis, A.M., Schachter, M.J., Gulati, S., Zitelli, K.T., Malanowski, S., Tajik, A., Fritz, C., Trulson, M., and Otte, S.L. (2018). Simultaneous optogenetics and cellular resolution calcium imaging during active behavior using a miniaturized microscope. Front Neurosci *12*, 496. 10.3389/fnins.2018.00496.
29. Zhang, J., Hughes, R.N., Kim, N., Fallon, I.P., Bakhurin, K., Kim, J., and Yin, H.H. (2021). All-optical imaging and patterned stimulation at cellular resolution with a one-photon endoscope. bioRxiv, 2021.12.19.473349. 10.1101/2021.12.19.473349.
30. Supekar, O.D., Sias, A., Hansen, S.R., Martinez, G., Peet, G.C., Peng, X., Bright, V.M., Hughes, E.G., Restrepo, D., Shepherd, D.P., et al. (2022). Miniature structured illumination microscope for in vivo 3D imaging of brain structures with optical sectioning. Biomed Opt Express *13*, 2530. 10.1364/boe.449533.
31. Göbel, W., Kerr, J.N.D., Nimmerjahn, A., and Helmchen, F. (2004). Miniaturized two-photon microscope based on a flexible coherent fiber bundle and a gradient-index lens objective. Opt Lett *29*, 2521. 10.1364/OL.29.002521.
32. Bao, H., Allen, J., Pattie, R., Vance, R., and Gu, M. (2008). Fast handheld two-photon fluorescence microendoscope with a 475 microm x 475 microm field of view for in vivo imaging. Opt Lett *33*, 1333–1335. 10.1364/OL.33.001333.
33. Helmchen, F., Denk, W., and Kerr, J.N.D. (2013). Miniaturization of two-photon microscopy for imaging in freely moving animals. Cold Spring Harb Protoc *2013*, 904–913. 10.1101/pdb.top078147.
34. Jung, J.C., and Schnitzer, M.J. (2003). Multiphoton endoscopy. Opt Lett *28*, 902–904. 10.1364/OL.28.000902.

35. Helmchen, F., Tank, D.W., and Denk, W. (2002). Enhanced two-photon excitation through optical fiber by single-mode propagation in a large core. Appl Opt *41*, 2930. 10.1364/ao.41.002930.
36. Udovich, J.A., Kirkpatrick, N.D., Kano, A., Tanbakuchi, A., Utzinger, U., and Gmitro, A.F. (2009). Spectral background and transmission characteristics of fiber optic imaging bundles. Appl Opt *47*, 4560. 10.1364/ao.47.004560.
37. Andresen, E.R., Sivankutty, S., Bouwmans, G., Gallais, L., Monneret, S., and Rigneault, H. (2015). Measurement and compensation of residual group delay in a multi-core fiber for lensless endoscopy. Journal of the Optical Society of America B *32*, 1221. 10.1364/josab.32.001221.
38. Leith, E.N., and Upatnieks, J. (1963). Wavefront Reconstruction with Continuous-Tone Objects*. J Opt Soc Am. 10.1364/josa.53.001377.
39. Qian, Y., Piatkevich, K.D., Mc Larney, B., Abdelfattah, A.S., Mehta, S., Murdock, M.H., Gottschalk, S., Molina, R.S., Zhang, W., Chen, Y., et al. (2019). A genetically encoded near-infrared fluorescent calcium ion indicator. Nat Methods. 10.1038/s41592-018-0294-6.
40. Dana, H., Sun, Y., Mohar, B., Hulse, B.K., Kerlin, A.M., Hasseman, J.P., Tsegaye, G., Tsang, A., Wong, A., Patel, R., et al. (2019). High-performance calcium sensors for imaging activity in neuronal populations and microcompartments. Nat Methods. 10.1038/s41592-019-0435-6.
41. Giovannucci, A., Friedrich, J., Gunn, P., Kalfon, J., Brown, B.L., Koay, S.A., Taxidis, J., Najafi, F., Gauthier, J.L., Zhou, P., et al. (2019). Caiman an open source tool for scalable calcium imaging data analysis. Elife *8*. 10.7554/eLife.38173.
42. Mathis, A., Mamidanna, P., Cury, K.M., Abe, T., Murthy, V.N., Mathis, M.W., and Bethge, M. (2018). DeepLabCut: markerless pose estimation of user-defined body parts with deep learning. Nat Neurosci. 10.1038/s41593-018-0209-y.
43. Antonini, A., Sattin, A., Moroni, M., Bovetti, S., Moretti, C., Succol, F., Forli, A., Vecchia, D., Rajamanickam, V.P., Bertoncini, A., et al. (2020). Extended field-of-view ultrathin microendoscopes for high-resolution two-photon imaging with minimal invasiveness. Elife *9*, 1–76. 10.7554/eLife.58882.
44. Wang, C., and Ji, N. (2013). Characterization and improvement of three-dimensional imaging performance of GRIN-lens-based two-photon fluorescence endomicroscopes with adaptive optics. Opt Express *21*, 27142–27154.
45. Accanto, N., Chen, I.-W., Ronzitti, E., Molinier, C., Tourain, C., Papagiakoumou, E., and Emiliani, V. (2019). Multiplexed temporally focused light shaping through a gradient index lens for precise in-depth optogenetic photostimulation. Sci Rep *9*, 7603. 10.1038/s41598-019-43933-w.
46. Andresen, V., Egner, A., and Hell, S.W. (2001). Time-multiplexed multifocal multiphoton microscope. Opt Lett *26*, 75. 10.1364/ol.26.000075.
47. Yu, J.Y., Kim, S., Shim, Y.B., Holland, D.B., Allodi, M.A., Yeh, C.Y., Blake, G.A., Han, Y.G., and Guo, C.L. (2018). Fiber-bundle illumination: realizing high-degree time-multiplexed multifocal multiphoton microscopy with simplicity. Sci Rep *8*, 14863. 10.1038/s41598-018-33286-1.
48. Zhang, T., Hernandez, O., Chrapkiewicz, R., Shai, A., Wagner, M.J., Zhang, Y., Wu, C.H., Li, J.Z., Inoue, M., Gong, Y., et al. (2019). Kilohertz two-photon

brain imaging in awake mice. Nat Methods *16*, 1119–1122. 10.1038/s41592-019-0597-2.
49. Podgorski, K., and Ranganathan, G. (2016). Brain heating induced by near-infrared lasers during multiphoton microscopy. J Neurophysiol *116*, 1012–1023. 10.1152/jn.00275.2016.
50. Iyer, V., Hoogland, T.M., and Saggau, P. (2006). Fast functional imaging of single neurons using random-access multiphoton (RAMP) microscopy. J Neurophysiol *95*, 535–545. 10.1152/jn.00865.2005.
51. Jennings, J.H., Kim, C.K., Marshel, J.H., Raffiee, M., Ye, L., Quirin, S., Pak, S., Ramakrishnan, C., and Deisseroth, K. (2019). Interacting neural ensembles in orbitofrontal cortex for social and feeding behaviour. Nature 2019, 1. 10.1038/s41586-018-0866-8.
52. Dalgleish, H.W.P., Russell, L.E., Packer, A.M., Roth, A., Gauld, O.M., Greenstreet, F., Thompson, E.J., and Häusser, M. (2020). How many neurons are sufficient for perception of cortical activity? Elife *9*, 1–99. 10.7554/eLife.58889.
53. Carrillo-Reid, L., Yang, W., Bando, Y., Peterka, D.S., and Yuste, R. (2016). Imprinting and recalling cortical ensembles. Science (1979) *353*, 691–694. 10.1126/science.aaf7560.
54. Robinson, N.T.M., Descamps, L.A.L., Russell, L.E., Buchholz, M.O., Bicknell, B.A., Antonov, G.K., Lau, J.Y.N., Nutbrown, R., Schmidt-Hieber, C., and Häusser, M. (2020). Targeted Activation of Hippocampal Place Cells Drives Memory-Guided Spatial Behavior. Cell *183*, 1586-1599.e10. 10.1016/j.cell.2020.09.061.
55. Bonifazi, P., Goldin, M., Picardo, M.A., Jorquera, I., Cattani, A., Bianconi, G., Represa, A., Ben-Ari, Y., and Cossart, R. (2009). GABAergic hub neurons orchestrate synchrony in developing hippocampal networks. Science (1979) *326*, 1419–1424. 10.1126/science.1175509.
56. Papagiakoumou, E., Ronzitti, E., and Emiliani, V. (2020). Scanless two-photon excitation with temporal focusing. Nat Methods *17*, 571–581. 10.1038/s41592-020-0795-y.
57. Accanto, N., Molinier, C., Tanese, D., Ronzitti, E., Newman, Z.L., Wyart, C., Isacoff, E., Papagiakoumou, E., and Emiliani, V. (2018). Multiplexed temporally focused light shaping for high-resolution multi-cell targeting. Optica *5*, 1478. 10.1364/OPTICA.5.001478.
58. Hernandez, O., Papagiakoumou, E., Tanese, D., Fidelin, K., Wyart, C., and Emiliani, V. (2016). Three-dimensional spatiotemporal focusing of holographic patterns. Nat Commun *7*, 11928. 10.1038/ncomms11928.
59. Flusberg, B.A., Nimmerjahn, A., Cocker, E.D., Mukamel, E.A., Barretto, R.P.J., Ko, T.H., Burns, L.D., Jung, J.C., and Schnitzer, M.J. (2008). High-speed, miniaturized fluorescence microscopy in freely moving mice. Nat Methods *5*, 935–938. 10.1038/nmeth.1256.
60. Zhang, T., Hernandez, O., Chrapkiewicz, R., Shai, A., Wagner, M.J., Zhang, Y., Wu, C.H., Li, J.Z., Inoue, M., Gong, Y., et al. (2019). Kilohertz two-photon brain imaging in awake mice. Nat Methods *16*, 1119–1122. 10.1038/s41592-019-0597-2.
61. Bovetti, S., Moretti, C., Zucca, S., Dal Maschio, M., Bonifazi, P., and Fellin, T. (2017). Simultaneous high-speed imaging and optogenetic inhibition in the intact mouse brain. Sci Rep *7*, 40041. 10.1038/srep40041.

62. Karigo, T., Kennedy, A., Yang, B., Liu, M., Tai, D., Wahle, I.A., and Anderson, D.J. (2020). Distinct hypothalamic control of same- and opposite-sex mounting behaviour in mice. Nature *589*, 258–263. 10.1038/s41586-020-2995-0.
63. Yu, K., Ahrens, S., Zhang, X., Schiff, H., Ramakrishnan, C., Fenno, L., Deisseroth, K., Zhao, F., Luo, M.H., Gong, L., et al. (2017). The central amygdala controls learning in the lateral amygdala. Nat Neurosci *20*, 1680–1685. 10.1038/s41593-017-0009-9.
64. Fratzl, A., Koltchev, A.M., Vissers, N., Tan, Y.L., Marques-Smith, A., Stempel, A.V., Branco, T., and Hofer, S.B. (2021). Flexible inhibitory control of visually-evoked defensive behaviour by the ventral lateral geniculate nucleus. Neuron. 10.1016/J.NEURON.2021.09.003.
65. Attardo, A., Fitzgerald, J.E., and Schnitzer, M.J. (2015). Impermanence of dendritic spines in live adult CA1 hippocampus. Nature *523*, 592–596. 10.1038/nature14467.
66. Meng, G., Liang, Y., Sarsfield, S., Jiang, W., Lu, R., Dudman, J.T., Aponte, Y., and Ji, N. (2019). High-throughput synapse-resolving two-photon fluorescence microendoscopy for deep-brain volumetric imaging in vivo. Elife *8*. 10.7554/eLife.40805.
67. Vierock, J., Rodriguez-Rozada, S., Dieter, A., Pieper, F., Sims, R., Tenedini, F., Bergs, A.C.F., Bendifallah, I., Zhou, F., Zeitzschel, N., et al. (2021). BiPOLES is an optogenetic tool developed for bidirectional dual-color control of neurons. Nat Commun *12*, 1–20. 10.1038/s41467-021-24759-5.
68. Adesnik, H., and Abdeladim, L. (2021). Probing neural codes with two-photon holographic optogenetics. Nat Neurosci *24*, 1356–1366. 10.1038/s41593-021-00902-9.
69. Guitchounts, G., Masís, J., Wolff, S.B.E., and Cox, D. (2020). Encoding of 3D Head Orienting Movements in the Primary Visual Cortex. Neuron *108*, 512-525.e4. 10.1016/j.neuron.2020.07.014.
70. Bouvier, G., Senzai, Y., and Scanziani, M. (2020). Head Movements Control the Activity of Primary Visual Cortex in a Luminance-Dependent Manner. Neuron *108*, 500-511.e5. 10.1016/j.neuron.2020.07.004.
71. Zahid, M., Vélez-Fort, M., Papagiakoumou, E., Ventalon, C., Angulo, M.C., and Emiliani, V. (2010). Holographic Photolysis for Multiple Cell Stimulation in Mouse Hippocampal Slices. PLoS One *5*, e9431-11.
72. Visser, T.D., and Oud, J.L. (1994). Volume measurements in three-dimensional microscopy. Scanning. 10.1002/sca.4950160403.
73. Binding, J., ben Arous, J., Léger, J.-F., Gigan, S., Boccara, C., and Bourdieu, L. (2011). Brain refractive index measured in vivo with high-NA defocus-corrected full-field OCT and consequences for two-photon microscopy. Opt Express. 10.1364/oe.19.004833.